

Observation of a chiral spin liquid phase of the Hubbard model on the triangular lattice: a density matrix renormalization group study

Aaron Szasz,^{1,2,*} Johannes Motruk,^{1,2} Michael P. Zaletel,^{3,1} and Joel E. Moore^{1,2}

¹*Department of Physics, University of California, Berkeley, California 94720, USA*

²*Materials Sciences Division, Lawrence Berkeley National Laboratory, Berkeley, California 94720, USA*

³*Department of Physics, Princeton University, Princeton, New Jersey 08540, USA*

(Dated: June 20, 2022)

Motivated by experimental studies that have found signatures of a quantum spin liquid phase in organic crystals whose structure is well described by the two-dimensional triangular lattice, we study the Hubbard model on this lattice at half filling using the infinite-system density matrix renormalization group (iDMRG) method. On infinite cylinders with finite circumference, we identify an intermediate phase between observed metallic behavior at low interaction strength and Mott insulating spin-ordered behavior at strong interactions. Chiral ordering from spontaneous breaking of time-reversal symmetry, a fractionally quantized spin Hall response, and characteristic level statistics in the entanglement spectrum in the intermediate phase provide strong evidence for the existence of a chiral spin liquid in the full two-dimensional limit of the model.

Quantum spin liquids^{1–3} have been the subject of considerable interest since the concept was first introduced in 1973 by Anderson, who suggested that geometrical frustration on the triangular lattice could lead to a resonating valence bond ground state of the antiferromagnetic Heisenberg model⁴. Although it is now known that the Heisenberg model on the triangular lattice in fact exhibits a three-sublattice 120° order in the ground state^{5,6}, antiferromagnetic models on the triangular lattice remain some of the most promising systems to realize a phase in which spins remain disordered even down to zero temperature. The triangular lattice has seemed particularly promising since the work of Shimizu *et al.*, who found that the organic crystal κ -(BEDT-TTF)₂Cu₂(CN)₃, which is well-described by independent 2D layers with nearly isotropic triangular lattice structure, shows no sign of spin-ordering even down to tens of mK, indicative of a possible spin liquid ground state⁷. Subsequent studies of this crystal have found that the heat capacity is T -linear at low temperature⁸, suggesting the presence of low-lying gapless excitations, but also that the thermal conductivity has no such T -linear contribution⁹, indicating to the contrary that there is a gap in the energy spectrum. The true nature of spin liquid phases in this and other triangular lattice materials such as EtMe₃Sb[Pd(dmit)₂]₂^{10–13} remains unclear.

Substantial theoretical effort has gone into answering this question, primarily in studying the antiferromagnetic Heisenberg model with additional terms, such as second-neighbor interactions and ring exchanges, that frustrate the expected three-sublattice order^{14–23}. The Heisenberg model and its extensions are derived from a perturbative expansion of a model of itinerant electrons, the Hubbard model²⁴; by studying the Hubbard model directly, we can capture additional effects that may be important in actual materials, at the cost of increased computational effort—compared with spin-1/2 models, the size of the local Hilbert space is doubled, so the system sizes that can be accessed by full-Hilbert-space numerical methods

are only about half as large.

Although there is now a wide variety of theoretical evidence pointing to the existence of a non-magnetic insulating phase of the triangular lattice Hubbard model^{14,25–33}, there is still little agreement on the precise nature of the phase. Some candidates, suggested by results on both the Hubbard and extended Heisenberg models, include a $U(1)$ spin liquid with a spinon Fermi sea^{14,15,18,31}, a nodal spin liquid^{17,29}, a gapped chiral spin liquid^{19,34–36}, and a \mathbb{Z}_2 spin liquid^{19,20}. In this work, we confirm the existence of a nonmagnetic insulating phase of the Hubbard model on the triangular lattice at half filling, provide strong evidence that it is a gapped chiral spin liquid, and comment on possible experimental signatures.

We study the triangular lattice Hubbard model on infinite cylinders with finite circumference using the density matrix renormalization group (DMRG) technique^{37–40}, a variational method to find the ground state of a Hamiltonian within the matrix product state (MPS) ansatz. This method has previously been applied to the Hubbard model on a triangular lattice two-leg ladder, providing evidence for a $U(1)$ spin liquid phase with a spinon Fermi surface³¹. For systems larger than the two-leg ladder, to our knowledge there exists only one prior paper³³ that uses DMRG to study the triangular lattice Hubbard model. The authors of that study used the finite-system DMRG to confirm the existence of a nonmagnetic insulating phase; in our infinite-system DMRG study, we study the nature of the phase by investigating the entanglement spectrum and the response to adiabatic spin-flux insertion through the cylinder.

The Model: The model we study is the standard Hubbard Hamiltonian,

$$H = -t \sum_{\langle ij \rangle \sigma} c_{i\sigma}^\dagger c_{j\sigma} + \text{H.c.} + U \sum_i n_{i\uparrow} n_{i\downarrow}, \quad (1)$$

where $c_{i\sigma}$ ($c_{i\sigma}^\dagger$) is the fermion annihilation (creation) operators for spin σ on site i and $n = c^\dagger c$ is the number operator; $\langle \cdot \rangle$ indicates nearest neighbor pairs on the tri-

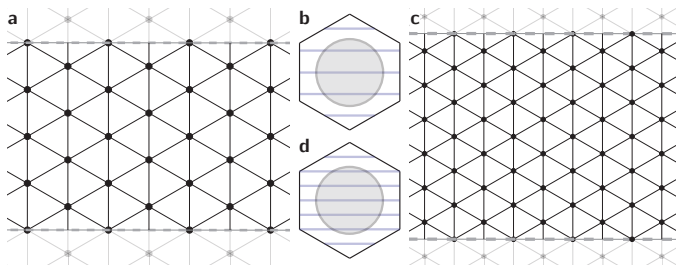


FIG. 1. (a) YC4 cylinder: the dashed lines are identified together and run along the length of the cylinder. (b) Horizontal lines show allowed momenta in the Brillouin zone for the YC4 cylinder. The shaded circle shows the Fermi surface at $U = 0$. (c) YC6 cylinder. (d) Allowed momenta for the YC6 cylinder.

angular lattice (Figure 1). We work at half filling, so that $\sum_i \langle n_{i\uparrow} + n_{i\downarrow} \rangle = N$, the total number of sites. This model has a single tunable parameter, U/t . In the limit $U = 0$, the model is exactly solvable and at half filling forms a metal with a circular Fermi surface (FS); in the limit $U \rightarrow \infty$, double occupancy is disallowed, so to lowest order in perturbation theory in t/U , the model reduces to the nearest-neighbor antiferromagnetic Heisenberg model²⁴, whose ground state exhibits a three-sublattice spin order^{5,6}. Between these two limits of $U = 0$ and $U \rightarrow \infty$ there must be at least one phase transition, from the metallic to the Mott-insulating phase; it is in the vicinity of this metal-insulator transition that a spin liquid phase is likely to be found.

To study this model using the DMRG method, we wrap the two-dimensional triangular lattice onto an infinitely long cylinder of finite circumference. We use the so-called YCn boundary conditions^{41,42}, for which one of the lattice vectors runs along the circumference of the cylinder. Denoting translation by one lattice constant around the cylinder by T_y , the YCn cylinder has a discrete translation symmetry $T_y^n = 1$; we explicitly conserve the momentum quantum numbers associated with this symmetry by rewriting the Hamiltonian in a mixed real- and momentum-space basis with single-particle operators $c_{x,k_y,\sigma}$, which both gives substantial improvements in computational efficiency and allows us to separately find the ground state in different momentum sectors.^{43,44} In this paper, we present results for the YC4 and YC6 cylinders, with four and six sites around the circumference respectively. The lattices are shown in Figures 1 (a) and (c), with the dashed gray lines identified together with periodic boundaries to form the cylinder. The finite circumference restricts the accessible momenta in the Brillouin zone as shown in Figures 1 (b) and (d).

Phase diagram: We first discuss how the various possible phases of the two-dimensional model should manifest on the infinite cylinders we study. A metallic state will be gapless, as indicated by a nonzero value for the central charge c of the corresponding one-dimensional conformal field theory; in particular, if the Fermi surface

intersects N_F of the allowed momentum lines in the Brillouin zone (see Figure 1 (b) and (d)), the central charge will be $c = 2N_F$ ^{42,45}. The 120-degree magnetically ordered phase will be fully gapped ($c = 0$) and symmetric on even circumference cylinders due to the integer-spin Haldane gap⁴⁶ induced by the reduced dimension, but the 2D spin-order should qualitatively manifest as large peaks in the spin-structure factor at the K^\pm points which diverge linearly with cylinder circumference. If the intermediate phase is a $U(1)$ spin liquid with a spinon Fermi surface, there will be a charge gap but no spin gap, leading to cylinder central charge $c = 2N_F - 1$ and $2k_F$ -singularities in the structure factors^{47,48}. Finally, a gapped spin liquid will have $c = 0$ and feature several “topologically-degenerate” low-lying states whose energy splitting decreases exponentially with circumference⁴⁹, along with other topological signatures we will return to in detail. The chiral spin liquid in particular will spontaneously break time reversal and parity symmetry, while retaining all others; time-reversal symmetry breaking is indicated by a nonzero scalar chiral order parameter $\langle \mathbf{S}_i \cdot (\mathbf{S}_j \times \mathbf{S}_k) \rangle$, where i, j , and k label the vertices of a triangle in the lattice⁵⁰. In the simulations, all these properties must be assessed as a function of the DMRG accuracy as captured by the bond-dimension χ of the MPS ansatz.

On the YC4 cylinder we find three phases, corresponding to the expected metallic, nonmagnetic insulating (NMI), and spin-ordered phases of the full two-dimensional model; the phase diagram and the evidence for it are summarized in Figure 2. The transition from the NMI phase to the spin-ordered phase at $U/t \approx 10.6$ is indicated by a peak in the correlation length, the appearance of large peaks near the K^\pm points of the Brillouin zone in the spin structure factor, and the vanishing of the chiral order parameter; the spin structure factor in particular allows us to identify the high- U side of this transition as the one-dimensional descendant of the two-dimensional magnetically ordered phase.

Because the metal is gapless, the metal to NMI transition ($U/t \approx 8$) is less obvious, but it can be observed from the destruction of the Fermi surface (see the Supplementary Material (SM)⁴²), and also from the chiral order parameter; although a nonzero value of the order parameter indicates time-reversal symmetry breaking in both the metallic and NMI phases for finite bond dimension, an extrapolation in the DMRG truncation error⁵¹ shows that the symmetry is actually unbroken in the low- U phase⁴². A further indication of the metal to NMI transition comes from finite entanglement scaling^{52–54}. If we cut the infinite cylinder into two semi-infinite halves, we can calculate the entanglement entropy S between them from the eigenvalues λ_i^2 of the reduced density matrix of either side of the cut,

$$S \equiv - \sum_i \lambda_i^2 \log(\lambda_i^2). \quad (2)$$

In the true ground state this is an infinite sum; however,

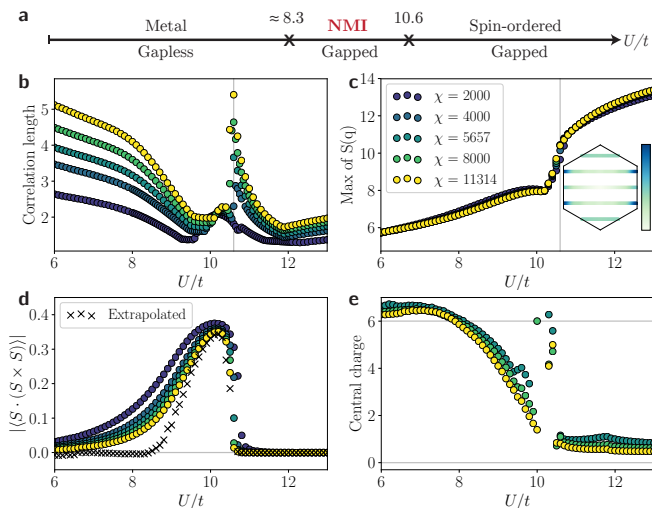


FIG. 2. (Color online) Results for the YC4 cylinder. In all panels, results are shown for a range of MPS bond dimensions χ as indicated in the upper right legend. (a) A nonmagnetic insulating (NMI) phase appears between a gapless metallic phase at low U/t and a magnetic phase at high U/t . (b) Correlation length. The vertical line at $U/t = 10.6$ is provided as a guide to the eye. (c) Spin structure factor: the curve shows the maximum value of the spin structure factor in the Brillouin zone. The inset shows the spin structure factor in the high- U phase, with peaks at the closest allowed momenta to the K^\pm points, where they would be expected for 120° magnetic ordering. Note that spin expectation values are reported here and throughout the paper with $\hbar/2 = 1$. (d) Chiral order parameter $\langle \mathbf{S}_i \cdot (\mathbf{S}_j \times \mathbf{S}_k) \rangle$, where i, j , and k label the three vertices of a triangle in the lattice, with an additional line showing extrapolation in the DMRG truncation error⁵¹; see the Supplementary Material⁴² for details. (e) Central charge of the effective one-dimensional state as calculated using finite entanglement scaling.

when running DMRG simulations the MPS bond dimension χ upper-bounds the number of non-zero λ_i in equation (2) and thereby bounds $S \leq \log(\chi)$. In a gapped state S is finite^{55,56}, so the DMRG estimate of S should converge as χ is increased. In a gapless state the true S is infinite, as is the correlation length ξ , but finite entanglement scaling predicts that the two quantities will scale with χ such that⁵⁷

$$S \approx (c/6) \log(\xi), \quad (3)$$

which can be used to estimate the central charge c of the conformal field theory corresponding to the gapless metallic phase.

We show the central charge computed using equation (3) in Figure 2(e). Until $U/t \approx 8$, the central charge is constant with respect to U/t and is near to the value $c = 6$ that we would expect for a metallic state^{42,45}. Beyond this point, the central charge begins to fall; although it remains nonzero at finite bond dimension, it is dropping rapidly with increasing χ , so we identify this as a gapped phase (see the SM for details⁴²). The appar-

ently unsystematic behavior near the previously identified transition at $U/t \approx 10.6$ is due to a slight shift in the location of the peak in the correlation length with bond dimension.

We can identify the location of this transition with more precision by studying the entanglement spectrum, which is the list of values $\{-\log(\lambda_i)\}$, for the same $\{\lambda_i\}$ appearing in equation (2). We observe that the entire spectrum acquires an exact two-fold degeneracy for $8.3 \lesssim U/t \lesssim 10.6$ and an exact four-fold degeneracy for $10.6 \lesssim U/t$ (see the SM for details⁴²), corresponding to the different projective representations of the symmetry group carried by the entanglement spectrum⁵⁸.

We also study the model on the YC6 cylinder. This lattice is depicted in Figure 1(c), and the allowed momenta in the Brillouin zone are shown in Figure 1(d). Because we employ a mixed real- and momentum-space basis, we can initialize the DMRG with states in different sectors of momentum around the cylinder per unit length⁵⁹, k , and thus separately find the ground state in each sector. On the YC4 cylinder, the ground state always lies in the $k = 0$ sector, but for the YC6 cylinder we observe low-lying states in two different momentum sectors, $k = 0$ and $k = \pi$. The relative energy difference between the ground states in the two sectors is shown in Figure 3(a). There are three apparent regimes of behavior: at low U , the $k = 0$ sector is clearly the ground state; at intermediate U , the two sectors become close in energy, and the difference is decreasing with bond dimension; at high U , the $k = \pi$ sector becomes the ground state, though again the relative difference in energy decreases with bond dimension.

The low- U phase is expected to be metallic, with central charge $c = 10$.^{42,45} Finite entanglement scaling indeed suggests that the phase is gapless⁴², though an accurate measurement of the central charge would require a bond dimension currently inaccessible to us, on the order of 50,000. (Extremely high entanglement in the low- U region leads to very large DMRG truncation error, on the order of 10^{-4} , even with $\chi \sim 10,000$.) The high- U phase should be the one-dimensional descendant of the two-dimensional 120° Néel ordered phase, and indeed at approximately the same value of U/t where the $k = \pi$ sector becomes the ground state, there is a rapid increase in peak height of the spin structure factor, as shown in Figure 3(b). In this phase, we observe the expected peaks in the structure factor at the corners of the Brillouin zone (lower right inset) and short range spin-ordering in the real-space spin-spin correlations (upper left inset).

The intermediate phase, for $U/t \approx 8$ to $U/t \approx 10$, is the region where the relative energy between the two momentum sectors is small and approximately constant; the spin structure factors are also approximately equal. We identify the transition to the right by the onset of the aforementioned spin ordering. To the left, the transition can be observed by the $k = 0$ sector becoming the sole ground state and from the transition in that sector to a

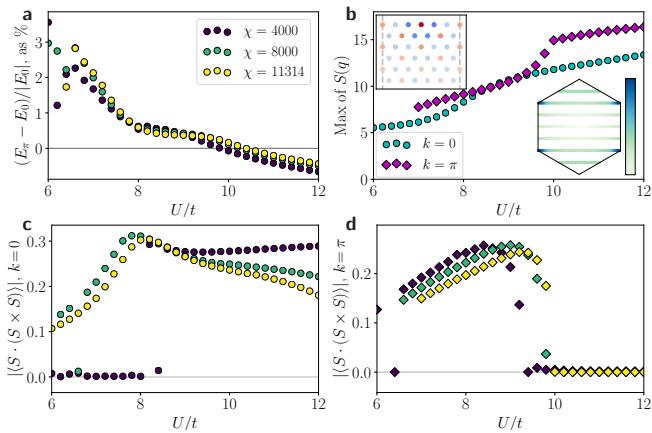


FIG. 3. (Color online) Results for the YC6 cylinder. (a) Relative energy (percent difference) between ground states in the symmetry sectors with $k = \pi$ and $k = 0$ around each ring. (b) Maximum value of the spin structure factor for the two momentum sectors. Insets show (lower right) the high- U spin structure factor for the $k = \pi$ sector, with peaks at the K^\pm points as expected for 120° magnetic ordering, and (upper left) the corresponding real-space $\langle \mathbf{S} \cdot \mathbf{S} \rangle$ correlations to a chosen point (center on the top). (c) Chiral order parameter for the $k = 0$ ground state. (d) Chiral order parameter for the $k = \pi$ ground state.

metallic phase, as can be seen qualitatively from the entanglement spectrum and finite entanglement scaling⁴². The scaling of S with χ suggests that the intermediate phase is gapped⁴², though we cannot access high enough bond dimensions to say so conclusively.

As with the YC4 cylinder, spontaneous breaking of time-reversal symmetry leads to a nonzero value of the chiral order parameter in the metallic and intermediate phases, as shown for the two momentum sectors in Figure 3 (c) and (d), though in the metal we would expect the symmetry to be restored at larger bond dimensions. In the $k = \pi$ sector, which is the true ground state for high U , the chiral order parameter rapidly vanishes at the spin-ordering transition.

Identification as a chiral spin liquid: We have demonstrated, for both the YC4 and YC6 cylinders, the existence of an intermediate phase which is nonmagnetic and which is clearly gapped for YC4 and very likely so for YC6. We now show that this phase can in fact be identified as a chiral spin liquid (CSL)^{34,50}.

A CSL is a topological phase with four degenerate ground states on the infinite cylinder⁶⁰. Each minimally entangled ground state⁶¹ spontaneously breaks time-reversal (T) and parity (P) symmetries, as indicated by a nonzero value of the chiral scalar order parameter; the two possible chiralities account for a two-fold degeneracy in the ground state manifold, which could be lifted by a P, T -breaking perturbation such as a magnetic field.

The remaining degeneracy is topological and is robust to such perturbations; the two topologically degenerate sectors, called the trivial and semion sectors, are distin-

guished by the respective absence or presence of a pair of semionic spinons, fractional excitations that carry spin- $1/2$ but no charge, separated to the ends of the cylinder at $\pm\infty$.^{60,62} In a pure spin system, insertion of 2π flux creates a pair of spinons and separates them to the ends of the cylinder, thus exchanging the two ground states and also pumping a net spin of exactly $1/2$ across any cut through the cylinder; this latter property indicates that the CSL has a spin Chern number of $1/2$ and a corresponding quantized spin Hall conductance⁶³.

In contrast, insertion of 2π spin-flux in the Hubbard model imposes antiperiodic boundary conditions on the cylinder, since $e^{2\pi i S^z} = -1$. The Hamiltonian is thus modified by 2π flux insertion, so that the question of whether the two ground state sectors are exchanged under flux insertion, as they are in a spin-model CSL, is ill-defined; instead, 2π flux insertion converts between one sector of the original Hamiltonian (with periodic boundaries) and the opposite sector of the Hamiltonian with antiperiodic boundaries, which should still lead to the same quantized spin pumping as for a spin model.

Each ground state of a CSL has a chiral edge mode with a universal low-lying spectrum; when the state is placed on an infinite cylinder, this edge spectrum appears in the entanglement spectrum for a cut between rings of the cylinder.^{64–66} The edge modes are described by a chiral $SU(2)_1$ Wess-Zumino-Witten (WZW) conformal field theory^{67,68}, labeling them by spin and momentum quantum numbers^{42,69}, for a given spin the number of levels at successive discrete momenta around the cylinder follows the counting $(1, 1, 2, 3, 5, \dots)$.⁷⁰ The spectrum is degenerate under $s_z \rightarrow -s_z$, where s_z is the spin quantum number of the entanglement level; the spin quantum numbers are integers in the trivial sector and half-integers in the semion sector, leading to two-fold degeneracy of the spectrum in the latter case.

We observe all of these signatures of the CSL phase. On the YC6 cylinder, we have already identified above two nearly degenerate low-lying states, in the $k = 0$ and $k = \pi$ momentum sectors; within each sector, by initializing the DMRG with different product states, we are able to converge to both chiralities (see SM⁴²), thus finding all four degenerate ground states. The chiral order parameter in each sector, indicative of time-reversal and parity symmetry-breaking, has already been shown above in Figures 3 (c) and (d); note that these figures show the absolute value of the order parameter, which is independent of the chirality to which the DMRG spontaneously converges.

The spin- and momentum-resolved entanglement spectra for the ground states in the two sectors are shown in Figure 4(a), where we have excluded levels corresponding to charge fluctuations between rings of the cylinder in order to highlight the spin degrees of freedom. Both spectra show the expected WZW level counting in the low-lying states, and the spin quantum numbers of the entanglement levels are integer for the $k = 0$ ground state and half-integer for $k = \pi$, allowing us to identify the

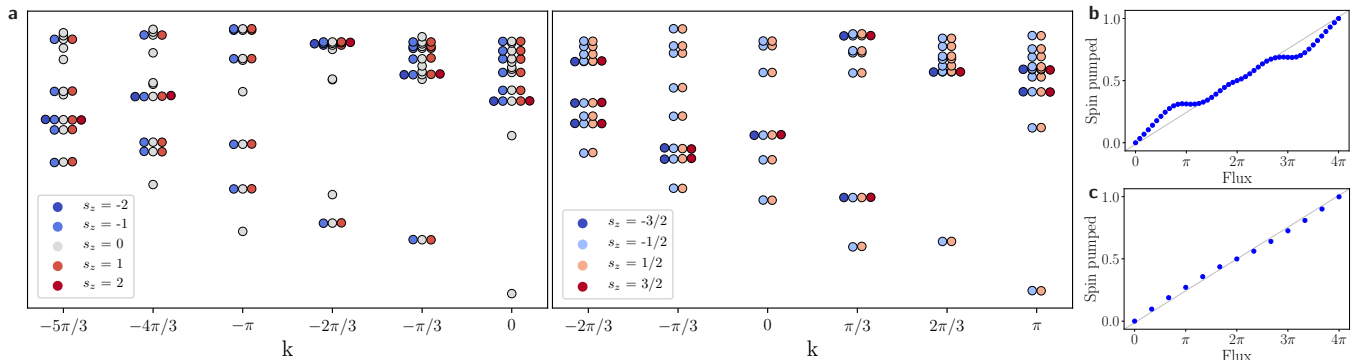


FIG. 4. (Color online) (a) Momentum- and spin-resolved entanglement spectrum for the YC6 cylinder in the intermediate phase, for the ground state in the $k = 0$ (left) and $k = \pi$ (right) sectors; these correspond to the trivial and semion sectors of a chiral spin liquid (CSL) respectively. Insertion of 2π flux interchanges the two topological sectors, though as discussed in the text there is a subtlety due to working with a fermion model. (b) Spin pumping as a function of flux insertion in the intermediate phase for YC4 ($U/t = 10$) and (c) YC6 ($U/t = 9$).

low-lying states in the two momentum sectors with the trivial and semion topological sectors respectively. For the corresponding results for the YC4 cylinder, see the SM⁴².

With flux insertion, we observe the quantized spin Hall effect, as shown for the YC4 and YC6 cylinders in Figures 4 (b) and (c) respectively, with a pumping of exactly spin $1/2$ per 2π flux insertion. The corresponding transformation of the entanglement spectrum with flux insertion is shown in the SM⁴²; as expected, 2π flux insertion converts between the two topological sectors.

Discussion: By employing DMRG to study the triangular lattice Hubbard model on infinite cylinders in a mixed real- and momentum-space basis, we have observed that the model exhibits three phases: a metallic phase, a nonmagnetic insulating phase, and a magnetically ordered phase. The intermediate phase shows the characteristic entanglement spectrum of a chiral spin liquid with two topologically degenerate ground state sectors and shows a fractionally quantized spin Hall effect. The phase additionally has a nonzero chiral order parameter and appears to be gapped. Collectively, this evidence strongly suggests that the nonmagnetic insulating phase is, in fact, a chiral spin liquid.

The apparent gapped nature of the spin liquid is consistent with the thermal conductivity measurements on κ -(BEDT-TTF)₂Cu₂(CN)₃ reported in reference 9. We find substantial disagreement with the past studies of this model using the DMRG method: the study on the two-leg ladder found a gapless spin liquid phase³¹, while the DMRG study on a finite XC6 cylinder⁴² found an intermediate phase that appeared gapped but with a rapidly decaying chiral-chiral correlation function³³. Both discrepancies may be explained by finite size effects, namely from the small system width in the former case and the use of finite cluster geometries in the latter.

It is important for future theoretical work to address the question of whether the chiral phase we find on the YC4 and YC6 cylinders indeed extrapolates to the full

two-dimensional model. The fact that cylinders of two different circumferences, one where the expected high- U magnetic order is allowed and one where it is geometrically frustrated, show essentially the same behavior in the intermediate phase suggests that it may survive in the two-dimensional limit. Further confirmation would be helpful, either by larger circumferences, which would be computationally expensive, or by fully 2D methods such as projected entangled pair states (PEPS)^{71,72}.

If our numerical findings indeed extrapolate to two dimensions, in real materials well described by the triangular lattice Hubbard model we would expect time-reversal symmetry to be broken below a finite temperature phase transition, with a thermal Hall response below the transition. At very low temperatures in a single-domain sample, we would observe a quantized thermal Hall conductance, $K_{xy} = \frac{\pi^2 k_B^2 T}{3h}$; note that this is twice the value of the Majorana-like plateau recently reported in α -RuCl₃⁷³. With disorder, there would be regions of both possible chiralities, with gapless edge modes between them; below the percolation threshold, this could lead simultaneously to the observed gapless behavior in the specific heat^{8,67} and gapped behavior seen in thermal transport measurements⁹.

An applied magnetic field could in principle break the degeneracy between the two chiralities, but this effect is extremely small at experimentally accessible field strengths. If the magnetic flux through a triangle in the lattice is ϕ , perturbation theory in t/U gives a term $[24(t^3/U^2)\sin(\phi)(\mathbf{S} \cdot (\mathbf{S} \times \mathbf{S}))]/h^3$ in the effective spin Hamiltonian; using our measured value for the chiral order parameter and estimated parameters for κ -(BEDT-TTF)₂Cu₂(CN)₃^{7,74}, in a 10 T field the energy splitting between ground states for the two chiralities is about 1 μ eV per lattice site, so at 1 K the favored chirality would be expected to be just 1% more prevalent. It is thus not surprising that experimental results⁸ do not see a significant effect from applied magnetic fields up to 10 T.

Acknowledgments: We would like to thank Bryan

Clark, Ryan Mishmash, Roger Mong, Frank Pollmann, Shigetoshi Sota, Senthil Todadri, Hiroshi Ueda, Ruben Verresen, and Seiji Yunoki for helpful conversations. We have also used the TenPy tensor network library⁷⁵, which includes contributions from MPZ, Mong, Pollmann, and others. Numerical computations were primarily performed using the Lawrence Livermore National Laboratory cluster at Lawrence Berkeley National Laboratory. This work was funded by the U.S. Department of Energy, Office of Science, Office of

Basic Energy Sciences, Materials Sciences and Engineering Division under Contract No. DE-AC02-05-CH11231 through the Scientific Discovery through Advanced Computing (SciDAC) program (KC23DAC Topological and Correlated Matter via Tensor Networks and Quantum Monte Carlo) (AS, MZ) and the Theory Institute for Materials and Energy Spectroscopies (TIMES) (JM). JM acknowledges support through DFG research fellowship MO 3278/1-1.

-
- * aszasz@berkeley.edu
- ¹ L. Balents, *Nature* **464**, 199 (2010).
 - ² L. Savary and L. Balents, *Reports on Progress in Physics* **80**, 016502 (2017).
 - ³ Y. Zhou, K. Kanoda, and T.-K. Ng, *Rev. Mod. Phys.* **89**, 025003 (2017).
 - ⁴ P. Anderson, *Materials Research Bulletin* **8**, 153 (1973).
 - ⁵ D. A. Huse and V. Elser, *Phys. Rev. Lett.* **60**, 2531 (1988).
 - ⁶ S. R. White and A. L. Chernyshev, *Phys. Rev. Lett.* **99**, 127004 (2007).
 - ⁷ Y. Shimizu, K. Miyagawa, K. Kanoda, M. Maesato, and G. Saito, *Phys. Rev. Lett.* **91**, 107001 (2003).
 - ⁸ S. Yamashita, Y. Nakazawa, M. Oguni, Y. Oshima, H. Nojiri, Y. Shimizu, K. Miyagawa, and K. Kanoda, *Nature Physics* **4**, 459 (2008).
 - ⁹ M. Yamashita, N. Nakata, Y. Kasahara, T. Sasaki, N. Yoneyama, N. Kobayashi, S. Fujimoto, T. Shibauchi, and Y. Matsuda, *Nature Physics* **5**, 44 (2008).
 - ¹⁰ T. Itou, A. Oyamada, S. Maegawa, M. Tamura, and R. Kato, *Phys. Rev. B* **77**, 104413 (2008).
 - ¹¹ T. Itou, A. Oyamada, S. Maegawa, M. Tamura, and R. Kato, *Journal of Physics: Conference Series* **145**, 012039 (2009).
 - ¹² M. Yamashita, N. Nakata, Y. Senshu, M. Nagata, H. M. Yamamoto, R. Kato, T. Shibauchi, and Y. Matsuda, *Science* **328**, 1246 (2010).
 - ¹³ T. Itou, A. Oyamada, S. Maegawa, and R. Kato, *Nature Physics* **6**, 673 (2010).
 - ¹⁴ O. I. Motrunich, *Phys. Rev. B* **72**, 045105 (2005).
 - ¹⁵ D. N. Sheng, O. I. Motrunich, and M. P. A. Fisher, *Phys. Rev. B* **79**, 205112 (2009).
 - ¹⁶ T. Grover, N. Trivedi, T. Senthil, and P. A. Lee, *Phys. Rev. B* **81**, 245121 (2010).
 - ¹⁷ R. V. Mishmash, J. R. Garrison, S. Bieri, and C. Xu, *Phys. Rev. Lett.* **111**, 157203 (2013).
 - ¹⁸ R. Kaneko, S. Morita, and M. Imada, *Journal of the Physical Society of Japan* **83**, 093707 (2014).
 - ¹⁹ W.-J. Hu, S.-S. Gong, W. Zhu, and D. N. Sheng, *Phys. Rev. B* **92**, 140403 (2015).
 - ²⁰ Z. Zhu and S. R. White, *Phys. Rev. B* **92**, 041105 (2015).
 - ²¹ S.-S. Gong, W. Zhu, J.-X. Zhu, D. N. Sheng, and K. Yang, *Phys. Rev. B* **96**, 075116 (2017).
 - ²² S. N. Saadatmand and I. P. McCulloch, *Phys. Rev. B* **96**, 075117 (2017).
 - ²³ Z. Zhu, P. A. Maksimov, S. R. White, and A. L. Chernyshev, *Phys. Rev. Lett.* **120**, 207203 (2018).
 - ²⁴ A. H. MacDonald, S. M. Girvin, and D. Yoshioka, *Phys. Rev. B* **37**, 9753 (1988).
 - ²⁵ P. Sahebsara and D. Sénéchal, *Phys. Rev. Lett.* **100**, 136402 (2008).
 - ²⁶ L. F. Tocchio, A. Parola, C. Gros, and F. Becca, *Phys. Rev. B* **80**, 064419 (2009).
 - ²⁷ T. Yoshioka, A. Koga, and N. Kawakami, *Phys. Rev. Lett.* **103**, 036401 (2009).
 - ²⁸ A. E. Antipov, A. N. Rubtsov, M. I. Katsnelson, and A. I. Lichtenstein, *Phys. Rev. B* **83**, 115126 (2011).
 - ²⁹ L. F. Tocchio, H. Feldner, F. Becca, R. Valentí, and C. Gros, *Phys. Rev. B* **87**, 035143 (2013).
 - ³⁰ M. Laubach, R. Thomale, C. Platt, W. Hanke, and G. Li, *Phys. Rev. B* **91**, 245125 (2015).
 - ³¹ R. V. Mishmash, I. González, R. G. Melko, O. I. Motrunich, and M. P. A. Fisher, *Phys. Rev. B* **91**, 235140 (2015).
 - ³² K. Misumi, T. Kaneko, and Y. Ohta, *Phys. Rev. B* **95**, 075124 (2017).
 - ³³ T. Shirakawa, T. Tohyama, J. Kokalj, S. Sota, and S. Yunoki, *Phys. Rev. B* **96**, 205130 (2017).
 - ³⁴ V. Kalmeyer and R. B. Laughlin, *Phys. Rev. Lett.* **59**, 2095 (1987).
 - ³⁵ W.-J. Hu, S.-S. Gong, and D. N. Sheng, *Phys. Rev. B* **94**, 075131 (2016).
 - ³⁶ A. Wietek and A. M. Läuchli, *Phys. Rev. B* **95**, 035141 (2017).
 - ³⁷ S. R. White, *Phys. Rev. Lett.* **69**, 2863 (1992).
 - ³⁸ S. R. White, *Phys. Rev. B* **48**, 10345 (1993).
 - ³⁹ S. Östlund and S. Rommer, *Phys. Rev. Lett.* **75**, 3537 (1995).
 - ⁴⁰ U. Schollwöck, *Annals of Physics* **326**, 96 (2011), January 2011 Special Issue.
 - ⁴¹ S. Yan, D. A. Huse, and S. R. White, *Science* **332**, 1173 (2011).
 - ⁴² See Supplemental Material below for further details.
 - ⁴³ J. Motruk, M. P. Zaletel, R. S. K. Mong, and F. Pollmann, *Phys. Rev. B* **93**, 155139 (2016).
 - ⁴⁴ G. Ehlers, S. R. White, and R. M. Noack, *Phys. Rev. B* **95**, 125125 (2017).
 - ⁴⁵ Philippe Francesco, Pierre Mathieu, and David Sénéchal, *Conformal Field Theory* (Springer-Verlag New York, 1997).
 - ⁴⁶ I. Affleck, *Journal of Physics: Condensed Matter* **1**, 3047 (1989).
 - ⁴⁷ D. N. Sheng, O. I. Motrunich, S. Trebst, E. Gull, and M. P. A. Fisher, *Phys. Rev. B* **78**, 054520 (2008).
 - ⁴⁸ S. D. Geraedts, M. P. Zaletel, R. S. K. Mong, M. A. Metlitski, A. Vishwanath, and O. I. Motrunich, *Science* **352**, 197 (2016).
 - ⁴⁹ X. G. Wen and Q. Niu, *Phys. Rev. B* **41**, 9377 (1990).
 - ⁵⁰ X. G. Wen, F. Wilczek, and A. Zee, *Phys. Rev. B* **39**, 11413 (1989).
 - ⁵¹ C. Hubig, J. Haegeman, and U. Schollwöck, *Phys. Rev. B*

- 97**, 045125 (2018).
- ⁵² L. Tagliacozzo, T. R. de Oliveira, S. Iblisdir, and J. I. Latorre, *Phys. Rev. B* **78**, 024410 (2008).
- ⁵³ F. Pollmann, S. Mukerjee, A. M. Turner, and J. E. Moore, *Phys. Rev. Lett.* **102**, 255701 (2009).
- ⁵⁴ B. Pirvu, G. Vidal, F. Verstraete, and L. Tagliacozzo, *Phys. Rev. B* **86**, 075117 (2012).
- ⁵⁵ M. B. Hastings, *Journal of Statistical Mechanics: Theory and Experiment* **2007**, P08024 (2007).
- ⁵⁶ I. Arad, A. Kitaev, Z. Landau, and U. Vazirani, ArXiv e-prints (2013), [arXiv:1301.1162 \[quant-ph\]](https://arxiv.org/abs/1301.1162).
- ⁵⁷ P. Calabrese and J. Cardy, *Journal of Statistical Mechanics: Theory and Experiment* **2004**, P06002 (2004).
- ⁵⁸ F. Pollmann, A. M. Turner, E. Berg, and M. Oshikawa, *Phys. Rev. B* **81**, 064439 (2010).
- ⁵⁹ M. P. Zaletel, Y.-M. Lu, and A. Vishwanath, *Phys. Rev. B* **96**, 195164 (2017).
- ⁶⁰ X. G. Wen, *Phys. Rev. B* **40**, 7387 (1989).
- ⁶¹ Y. Zhang, T. Grover, A. Turner, M. Oshikawa, and A. Vishwanath, *Phys. Rev. B* **85**, 235151 (2012).
- ⁶² M. Oshikawa and T. Senthil, *Phys. Rev. Lett.* **96**, 060601 (2006).
- ⁶³ S.-S. Gong, W. Zhu, and D. N. Sheng, *Scientific Reports* **4**, 6317 (2014).
- ⁶⁴ A. Kitaev and J. Preskill, *Phys. Rev. Lett.* **96**, 110404 (2006).
- ⁶⁵ H. Li and F. D. M. Haldane, *Phys. Rev. Lett.* **101**, 010504 (2008).
- ⁶⁶ X.-L. Qi, H. Katsura, and A. W. W. Ludwig, *Phys. Rev. Lett.* **108**, 196402 (2012).
- ⁶⁷ X. G. Wen, *Phys. Rev. B* **43**, 11025 (1991).
- ⁶⁸ L. Cincio and G. Vidal, *Phys. Rev. Lett.* **110**, 067208 (2013).
- ⁶⁹ M. P. Zaletel, R. S. K. Mong, and F. Pollmann, *Phys. Rev. Lett.* **110**, 236801 (2013).
- ⁷⁰ J. E. Moore and F. D. M. Haldane, *Phys. Rev. B* **55**, 7818 (1997).
- ⁷¹ F. Verstraete and J. I. Cirac, eprint [arXiv:cond-mat/0407066](https://arxiv.org/abs/cond-mat/0407066) (2004), [cond-mat/0407066](https://arxiv.org/abs/cond-mat/0407066).
- ⁷² P. Corboz, R. Orús, B. Bauer, and G. Vidal, *Phys. Rev. B* **81**, 165104 (2010).
- ⁷³ Y. Kasahara, T. Ohnishi, Y. Mizukami, O. Tanaka, S. Ma, K. Sugii, N. Kurita, H. Tanaka, J. Nasu, Y. Motome, T. Shibauchi, and Y. Matsuda, ArXiv e-prints (2018), [arXiv:1805.05022 \[cond-mat.str-el\]](https://arxiv.org/abs/1805.05022).
- ⁷⁴ T. Komatsu, N. Matsukawa, T. Inoue, and G. Saito, *Journal of the Physical Society of Japan* **65**, 1340 (1996).
- ⁷⁵ J. A. Kjäll, M. P. Zaletel, R. S. K. Mong, J. H. Bardarson, and F. Pollmann, *Phys. Rev. B* **87**, 235106 (2013).

Supplementary Material for: Observation of a chiral spin liquid phase of the Hubbard model on the triangular lattice: a density matrix renormalization group study

Aaron Szasz,^{1,2,*} Johannes Motruk,^{1,2} Michael P. Zaletel,^{3,1} and Joel E. Moore^{1,2}

¹*Department of Physics, University of California, Berkeley, California 94720, USA*

²*Materials Sciences Division, Lawrence Berkeley National Laboratory, Berkeley, California 94720, USA*

³*Department of Physics, Princeton University, Princeton, New Jersey 08540, USA*

(Dated: August 1, 2018)

I. COMPACTIFICATION TO A CYLINDER

As described in the main text, we use the density matrix renormalization group (DMRG) method to study the Hubbard model on the triangular lattice^{1,2}. The DMRG is a method for finding the ground state of a one-dimensional model, so it cannot be used to study the full two-dimensional system directly. Instead, we take 1D strips of the lattice with some finite width. In particular, we identify the two edges of the strip with each other, using periodic boundary conditions; this eliminates edge effects, giving the best approximation to the 2D model that we can achieve with a strip of finite width.

To pick the 1D strip that defines the cylinder, we follow these steps:

1. Pick two points of the lattice, and declare them to be equivalent.
2. The line between the two points is the width of the strip or equivalently the circumference of the cylinder.
3. The line passing through the identified point (ie both points, since they are the same) and perpendicular to the circumference is the glued edge of the cylinder.

It is important to note that choosing any cylinder of this type automatically guarantees periodicity of the Hamiltonian along the cylinder, so we once again have a translation-invariant system. To see this, let the lattice vectors \mathbf{a} and \mathbf{b} be as shown in Figure 1, and a the lattice spacing. Then, noting that $\mathbf{a}^2 = \mathbf{b}^2 = a^2$ and $\mathbf{a} \cdot \mathbf{b} = a^2/2$, if the edges are perpendicularly separated by $n_a\mathbf{a} + n_b\mathbf{b}$ for some integers n_a and n_b (as must be true given the above procedure), then one can check that the vector $(2n_b + n_a)\mathbf{a} - (2n_a + n_b)\mathbf{b}$ is perpendicular, and both coefficients are integers. This is a vector that points along the length of the cylinder, and it is an integer linear combination of the lattice vectors, so the Hamiltonian is invariant under this translation. (In some cases, the actual period may be smaller than this, eg if $n_b = 0$ and n_a is even.)

A. Allowed cylinders and the consequences of choosing one

We now have a general procedure for generating cylinders to which the 2D triangular lattice Hubbard Hamiltonian can be restricted in a natural way, namely by picking pairs of points on the lattice to identify with each other. If

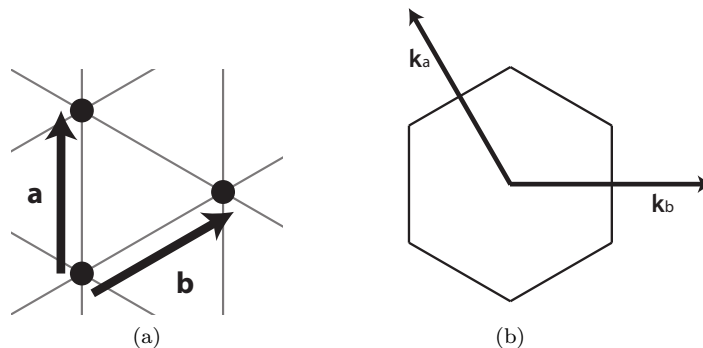


FIG. 1. (a) Lattice vectors \mathbf{a} and \mathbf{b} on the triangular lattice. (b) Corresponding reciprocal lattice vectors and the first Brillouin zone.

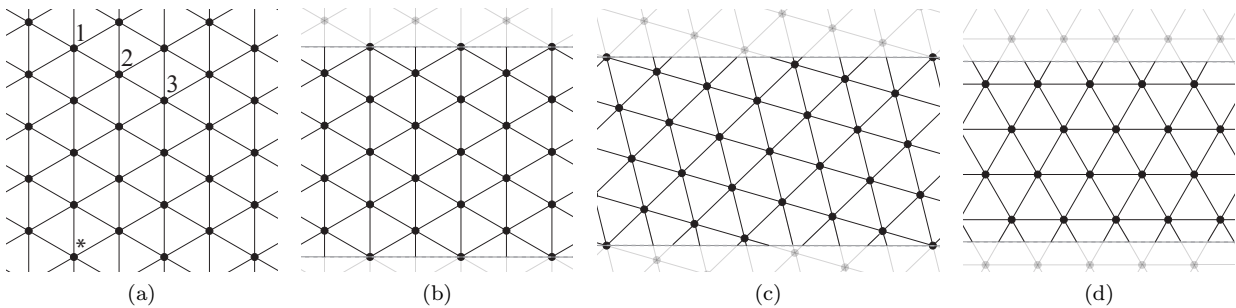


FIG. 2. (a) Periodic boundary conditions on the cylinder are defined by identifying the point \star with the points labeled in the figure as 1, 2 and 3, which correspond to $(n_a, n_b) = (4, 0)$, $(3, 1)$, and $(2, 2)$ respectively. (b) Cylinder from identifying point \star with point 1, called YC4 boundary conditions. This is the same cylinder one would get by adding sites at the hexagon centers of a zigzag nanotube. (c) Cylinder from identifying point \star with point 2. Note that this case has a 26-site unit cell, making it computationally intractable. (d) Cylinder from identifying point \star with point 3, called XC4 boundary conditions. This corresponds to adding sites at the hexagon centers of an armchair nanotube.

we fix the cylinder circumference (in Manhattan distance, ie the minimum number of lattice vectors to go between equivalent points; this is not the physical circumference in general) to be a particular integer, L , there are exactly $\lfloor (L+1)/2 \rfloor$ unique cylinders of this type that can be constructed, which are given by fixing one point in the 2D lattice and identifying it with each of the $\lfloor (L+1)/2 \rfloor$ points separated by $n_a \mathbf{a} + n_b \mathbf{b}$ such that $n_a + n_b = L$ and $n_a \in \{ \lfloor L/2 \rfloor, \lfloor L/2 \rfloor + 1, \dots, L \}$. The three points for $n = 4$ are shown in Figure 2a. All other lattice points that are equidistant (in Manhattan distance) from the fixed point give physically equivalent cylinders by rotating or reflecting the 2D lattice. The resulting one-dimensional strips (with a cylinder formed by identifying the edges) are shown in Figures 2b, 2c, and 2d; the first and third cylinders are called YC4 and XC4, indicating that a lattice vector runs, respectively, along the y or the x direction³. In general, the YCL cylinder is one with $(n_a, n_b) = (L, 0)$ and is defined for any L , while the XCL cylinder can be constructed only when L is even and corresponds to $(n_a, n_b) = (L/2, L/2)$.

The choice of boundary conditions has important consequences, both for the physics of the model and for the computational efficiency of the DMRG. The first implication of the choice of boundary conditions is that the allowed momenta in the Brillouin zone are restricted. The allowed inequivalent momenta in the full 2D model are those in the first Brillouin zone, which is shown for this model in Figure 3a. However, if we define a cylinder by identifying, with periodic boundary conditions, two points that are separated by $n_a \mathbf{a} + n_b \mathbf{b}$, then an eigenstate at momentum $\mathbf{k} = c_a \mathbf{k}_a + c_b \mathbf{k}_b$ (c_a and c_b can be arbitrary real numbers) must satisfy $\psi_{\mathbf{k}}(\mathbf{x}) = \psi_{\mathbf{k}}(\mathbf{x} + n_a \mathbf{a} + n_b \mathbf{b})$, or equivalently (due to Bloch's theorem)

$$1 = e^{i(n_a \mathbf{a} + n_b \mathbf{b}) \cdot (c_a \mathbf{k}_a + c_b \mathbf{k}_b)} = e^{2\pi i(n_a c_a + n_b c_b)} \quad (1)$$

which requires that $n_a c_a + n_b c_b$ be an integer. Each integer corresponds to a particular line through the Brillouin zone. For example, in the case of the YC4 cylinder, where $n_a = 4$ and $n_b = 0$, there is no restriction on c_b but c_a must be an integer multiple of $1/4$. This leads to the cuts through Brillouin zone shown in Figure 3b. The corresponding cuts for the other two possible choices of boundary conditions are shown in Figures 3c and 3d.

A related consequence of the choice of boundary conditions is that certain types of multi-sublattice orders may or may not be allowed. This is extremely important for the triangular lattice Hubbard model, which in the limit $U \rightarrow \infty$ reduces to the nearest neighbor Heisenberg model and thus should have a three-sublattice 120° Néel order. Notably, this order is *not allowed* on the YC4 cylinder, since the four sites around the circumference cannot be assigned to three distinct sublattices in a consistent way.

Another physical consequence of the choice of boundary condition is that the final cylinder circumference can vary in size. In the case of YC4 boundaries, the cylinder has circumference $4a$, while for XC4 boundaries it is just $2\sqrt{3}a$. This is also reflected in total length of the allowed cuts through the Brillouin zone; these have lengths $4 \times (4\pi/a\sqrt{3})$ and $2\sqrt{3} \times (4\pi/a\sqrt{3})$ respectively. This means that with a given number of sites L in the unit cell, the YCL cylinder may be “more two-dimensional” than the corresponding XCL cylinder, though this effect is presumably less important than the question of which multi-sublattice orders are or are not allowed.

Finally, an appropriate choice of boundary conditions can dramatically speed up numerical computations by introducing additional conserved quantities. The YCL cylinders have discrete L -fold translation symmetry around the cylinder, leading to L conserved momenta. These correspond to the cuts through the Brillouin zone. The XCL cylinders (well-defined for even L) similarly have $L/2$ -fold discrete translation symmetry, giving $L/2$ conserved quantities.

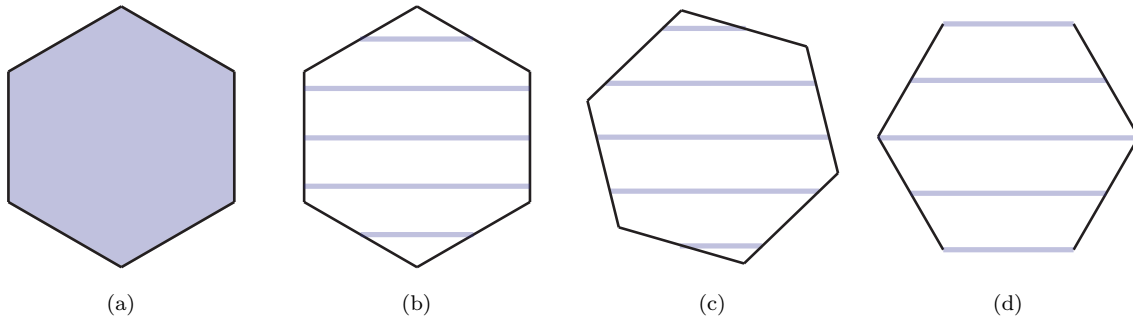


FIG. 3. (a) Allowed momenta in the first Brillouin zone of the full 2D triangular lattice. (b) Allowed momenta for YC4 boundary conditions. (c) Allowed momenta for the $(n_a, n_b) = (3, 1)$ boundary conditions. (d) Allowed momenta for the XC4 boundary conditions. Note that in (b)-(d), if the hexagons are tiled, then the allowed cuts form 4, 1, and 2 distinct lines respectively, corresponding to different numbers of conserved momenta in the Hamiltonian.

The distinct conserved momenta correspond to distinct allowed cuts through the Brillouin zone (figure 3): if the BZ is tiled, then the allowed cuts actually form 4, 1, and 2 distinct lines for the three respective boundary conditions.

As explained in the main text, we perform all calculations using the YC boundary conditions (specifically YC4 and YC6). There are two main reasons: (1) by choosing different cylinder circumferences, we can try to stabilize/destabilize different phases and in particular we can frustrate the expected high- U magnetic order to make a spin liquid phase more robust and easier to observe; and (2) with YCL boundary conditions we can use a mixed real- and momentum-space basis with L conserved momenta, which both gives a dramatic improvement in computational efficiency and allows us to separately find the ground state in different momentum sectors.

II. EXPECTED CENTRAL CHARGE IN THE METALLIC PHASE

As reported in the main text, we numerically observe for the YC4 cylinder a central charge $c \approx 6$. This is the expected result for the metallic phase, based on an exact tight-binding solution for the non-interacting limit of $U = 0$ on the full 2D lattice. In that limit, the Hamiltonian becomes:

$$H = -2t \sum_{kq\sigma} n_{kq\sigma} (\cos(2\pi k a) + \cos(2\pi q a) + \cos(2\pi(k - q)a)) \quad (2)$$

where the momentum in the Brillouin zone is given by $\mathbf{k} = k\mathbf{k}_a + q\mathbf{k}_b$ for the reciprocal lattice vectors \mathbf{k}_a and \mathbf{k}_b as shown in Figure 1(b). In the ground state, all states with negative energy will be occupied and all with positive energy will be empty, defining a circular Fermi surface with radius $2\pi/(3a)$.

When the system is restricted to a finite cylinder, we can then count how many of the allowed momentum cuts cross the Fermi surface. This is shown visually in Figure 4 for the YC4 and YC6 cylinders; the number of cuts crossing the Fermi surface is 3 for YC4 and 5 for YC6.

Each distinct cut through the Fermi surface corresponds to two species of free fermion, one for spin up and one for spin down, and each free fermion contributes a central charge of 1⁴. Thus we conclude that the expected central charges at $U = 0$ and therefore throughout the metallic phase are 6 and 10 for the YC4 and YC6 cylinders, respectively.

III. YC4 CHIRAL ORDER PARAMETER AND EXTRAPOLATION

In Figure 2(d) of the main text, we show the chiral order parameter $\langle \mathbf{S}_i \cdot (\mathbf{S}_j \times \mathbf{S}_k) \rangle$, where i, j , and k label three lattice sites at the vertices of a triangle, as a function of U/t at different bond dimensions. We additionally show an extrapolation in the DMRG truncation error; here we explain the details of the extrapolation method.

At each value of U/t , we have values of the order parameter for five different bond dimensions, namely 2000, 4000, $5657 \approx 4000\sqrt{2}$, 8000, and $11314 \approx 8000\sqrt{2}$, and corresponding DMRG truncation errors, p . The error in the energy of a state should scale linearly with the truncation error, $E = E_{\text{lim}} + A \times p$,⁵ but the error in other observables may scale in a more complicated manner. For the chiral order parameter, we assume a scaling of the form

$$\langle \mathbf{S}_i \cdot (\mathbf{S}_j \times \mathbf{S}_k) \rangle = \langle \mathbf{S}_i \cdot (\mathbf{S}_j \times \mathbf{S}_k) \rangle_{\text{lim}} + A \times p^B \quad (3)$$

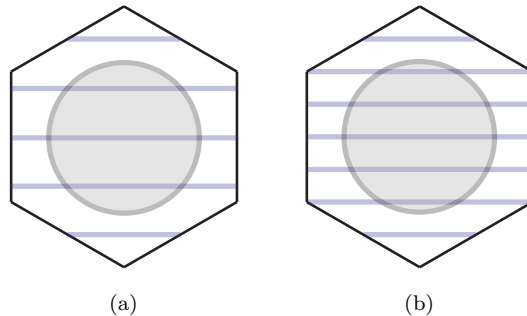


FIG. 4. **(a)** The shaded circle denotes single-particle eigenstates that are filled in the $U = 0$ limit of the model on the full two-dimensional lattice. The blue lines are the allowed momentum cuts for the YC4 cylinder; evidently, three of them cross the Fermi surface. **(b)** Same for the YC6 cylinder, with 5 lines crossing the Fermi surface.

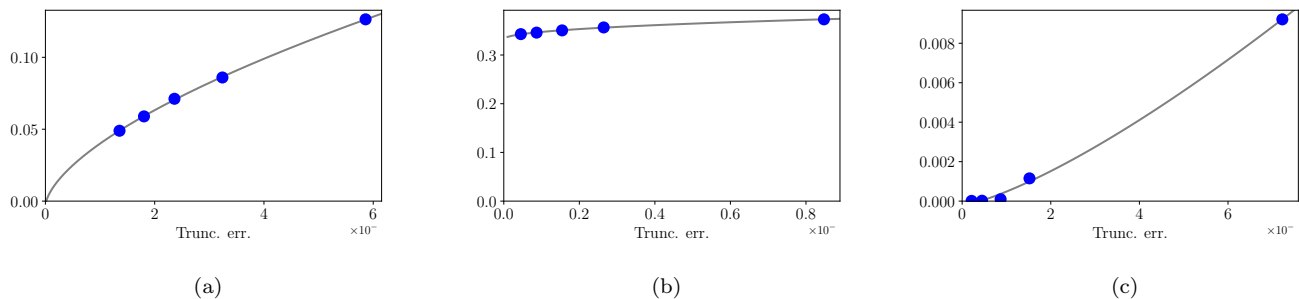


FIG. 5. Chiral order parameter versus DMRG truncation error, for **(a)** $U/t = 8$ in the low- U phase, **(b)** $U/t = 10$ in the intermediate phase, and **(c)** $U/t = 11$ in the high- U phase. Gray lines show best fit curves of the form $C + A \times p^B$, allowing for extrapolation to the limit of no truncation error/infinite bond dimension.

used in reference 5, Figure 8. The data and best fit curves for several specific values of U/t are shown in Figure 5; in particular, we show $U/t = 8$ at the upper end of the metallic phase, $U/t = 10$ where the chiral order parameter is near its peak, and $U/t = 11$ in the high- U phase. (The `optimize.curve_fit` function from Python's `scipy` library fails to find the best fit of this form for $U/t \gtrsim 11.5$, beyond which we use instead a linear extrapolation from the few highest bond dimensions.)

We also show in Figure 6 the best fit results if we do a simple linear extrapolation from the three highest bond dimensions; we show the best fit line with the data for $U/t = 8$ and $U/t = 10$, as well as the equivalent of Figure 2(d) from the main text with the extrapolation line determined using this linear fit. (The best linear fit at $U/t = 11$ is simply a flat line at 0.) This method makes it seem that some time-reversal symmetry breaking may survive in the low- U phase, but comparing the fitted curves for $U/t = 8$ using the two methods, it appears that the nonlinear fit is significantly better, and that one predicts the expected vanishing of the chiral order parameter in the low- U phase.

Despite the disagreement at low U , in intermediate phase the two extrapolation methods give essentially similar results, as seen in Figures 5b and 6b; the chiral order clearly remains nonzero in the limit of infinite bond dimension/zero truncation error.

IV. DESTRUCTION OF THE FERMI SURFACE AT METAL-INSULATOR TRANSITION

One sign of a metallic, or Fermi liquid, state is the presence of a singularity at the Fermi surface in the occupation $\langle n_k \rangle$. We do not observe a singularity at any finite MPS bond dimension, but by measuring $\langle n_k \rangle$ as a function of U/t and bond dimension we can observe the approximate location where the singularity would appear. We perform this computation for the YC4 cylinder.

We compute the correlators $\langle c_{0,k_y,\uparrow}^\dagger c_{x,k_y,\uparrow} \rangle$ for x in the range -50 to 50 , then compute the occupation for spin up

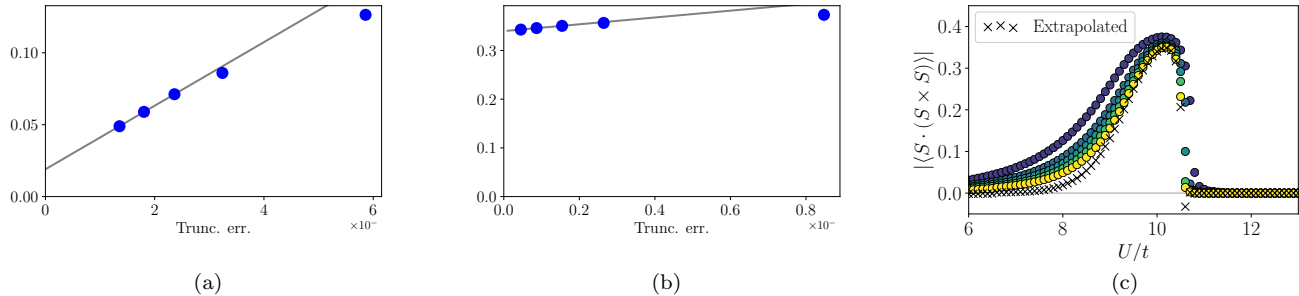


FIG. 6. In (a) and (b), we show the same data as in Figures 5a and 5b respectively, but with linear best fit lines computed using the points with the three lowest truncation errors in each case. The result is essentially unchanged in the intermediate phase. In (c), we show the extrapolation as a function of U/t using this linear fit method. The actual data is the same as in Figure 2(d) of the main text.

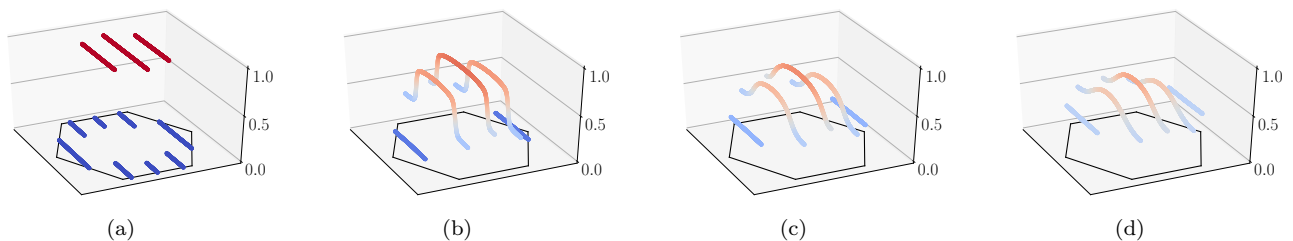


FIG. 7. Spin up occupation in the Brillouin zone, $\langle n_{k\uparrow} \rangle$, for (a) $U/t = 0$ (exact result), (b) $U/t = 6$ in the metallic phase, (c) $U/t = 9$ in the spin liquid phase, and (d) $U/t = 12$ in the high- U phase.

by

$$\langle n_{k_x, k_y, \uparrow} \rangle = \sum_{x=-50}^{50} e^{ik_x x} \langle c_{0, k_y, \uparrow}^\dagger c_{x, k_y, \uparrow} \rangle. \quad (4)$$

The range of 50 is about an order of magnitude larger than the correlation length, and the results are converged in the sense that when $\langle n_{k\uparrow} \rangle$ is plotted, the curves from using 40 vs 50 points are essentially indistinguishable.

In Figure 7 we show the spin up occupation in the Brillouin zone (computed with bond dimension $\chi = 4000$) for $U/t = 6$ in the metallic phase, $U/t = 9$ in the spin liquid phase, and $U/t = 12$ in the high- U phase, as well as the exact tight-binding result for $U = 0$ as a comparison. The behavior is clearly qualitatively different at high U compared with low U .

To make the transition more evident, we also show the maximum gradient of the occupation vs U/t for several bond dimensions in Figure 8a. If there is indeed a singularity in the limit of infinite bond dimension, the maximum gradient should extrapolate to infinity, which appears to be the case at $U/t = 6$. If, on the other hand, there is no singularity, then the gradient should converge as the bond dimension increases, which is clearly the case for $U/t \gtrsim 10$. The exact location of the transition remains unclear, however, since for $8 \lesssim U/t \lesssim 10$, it is not clear whether the gradient will diverge or not.

Another possibility for observing the transition is to add a factor of $|x|$ in the Fourier transform in equation (4), which converts the singularity at the Fermi surface into a peak. We can then plot the peak height, which is shown in Figure 8b. This allows for a somewhat more precise determination of the transition location, at $U/t \approx 8.5$.

V. FINITE ENTANGLEMENT SCALING FOR YC4

In the main text, we show in Figure 2(e) the central charge, a characteristic property of the conformal field theory describing a gapless one dimensional system, computed as a function of U/t using the scaling relation⁶

$$S \approx (c/6) \log(\xi). \quad (5)$$

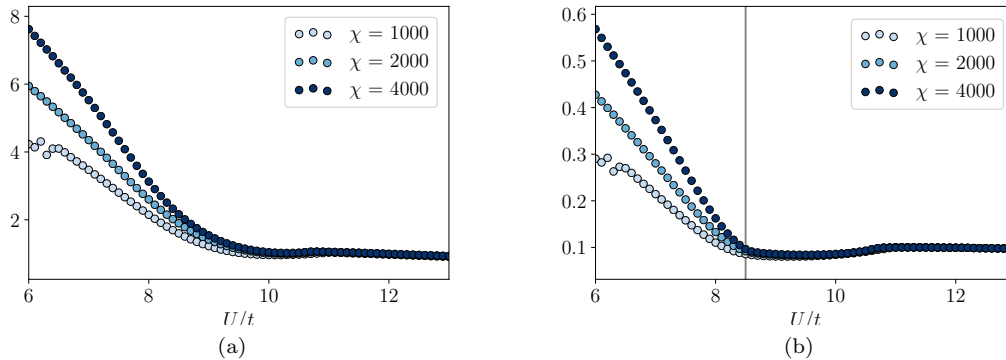


FIG. 8. **(a)** Maximum gradient of the occupation, as a function of U/t and bond dimension, showing a transition between $U/t \approx 8$ and $U/t = 10$. **(b)** Height of the peak at the Fermi surface found by including a factor of $|x|$ in the Fourier transform in equation 4. The vertical line at $U/t = 8.5$ appears to be the approximate location of the transition.

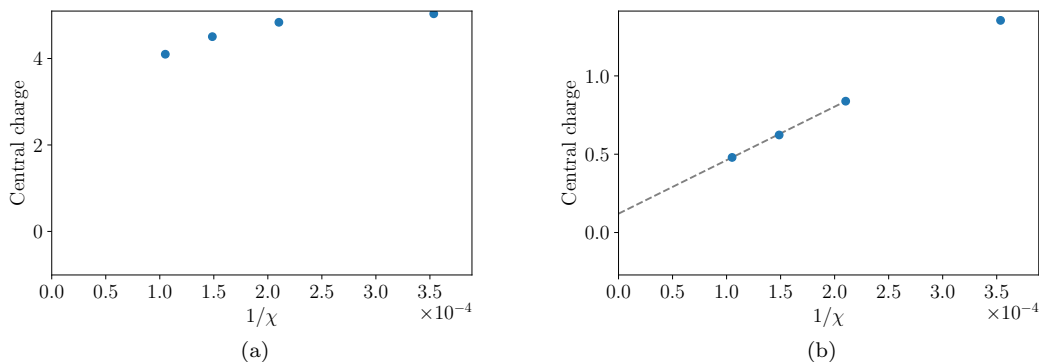


FIG. 9. Central charge vs $1/\chi$ for **(a)** $U/t = 9$ and **(b)** $U/t = 13$. Both seem to extrapolate to finite values, but this is misleading, as discussed in the text.

From these results, it is clear that there is a finite central charge at low U , with a value of approximately $c = 6$, which is exactly what we expect for a metallic state on this cylinder as discussed in section II above. The behavior in the intermediate and high- U phases is less obvious, but here we show that our data suggest that $c = 0$ in both of those phases, indicating that they are gapped.

It will be helpful to first explain further the precise way that we calculate the central charge. At each U/t and each bond dimension, we can calculate the total entanglement entropy S for a cut between two rings of the cylinder, and also the correlation length (Figure 2(b) of the main text). As both become large, they should scale according to equation (5), but the relation will be inaccurate when both quantities are small. The coefficient is thus best approximated by the derivative, $c/6 \approx d \log(\xi)/dS$, and we calculate discrete approximations to this derivative from the values of S and ξ at successive bond dimensions; the lines in Figure 2(e) of the main text are labeled by the larger of the two bond dimensions used in calculating the discretized derivative. So for example the yellow (most accurate) line in the figure is computed using the ground state wave functions for bond dimensions 8000 and 11314.

In Figure 9, we show the central charge estimates at $U/t = 9$ and at $U/t = 13$ versus $1/\chi$, where the χ used is the geometric mean of the two bond dimensions used to calculate the derivative. In the high- U phase we show a linear extrapolation to infinite bond dimension; although it appears to show a small but nonzero central charge, that is not really a reliable result. For example, the use of the geometric mean of the two bond dimensions used is an arbitrary choice, particularly because the error may be determined mostly by the smaller bond dimension, and using that bond dimension for the horizontal axis would shift the graph to the right. At $U/t = 9$, it is essentially impossible to extrapolate the central charge at all as the shape of the curve is completely unclear.

Given the lack of clarity from these extrapolations, we can take a different approach to calculating the central charge in the intermediate and high- U phases. In both phases, and particularly in the high- U phase, the entanglement appears

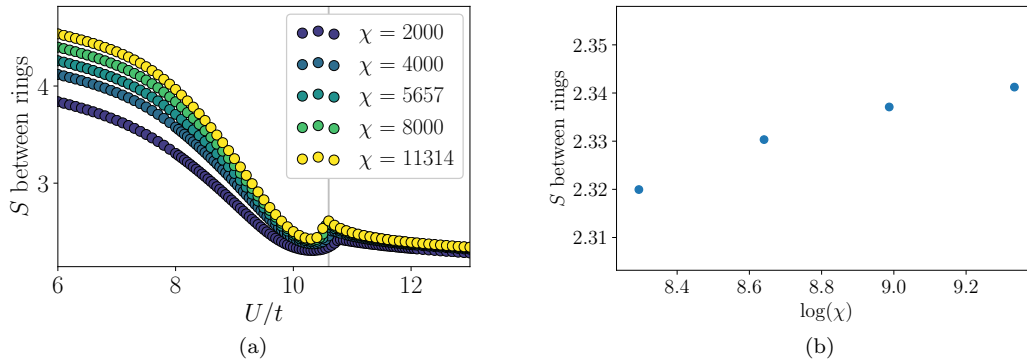


FIG. 10. (a) Entanglement between rings of the cylinder as a function of U/t for different bond dimensions. It is nearly converged in the intermediate and high- U phases, indicating that they are gapped. (b) A close-up slice at $U/t = 13$. Note that the vertical scale is only about 2% of the value of S .

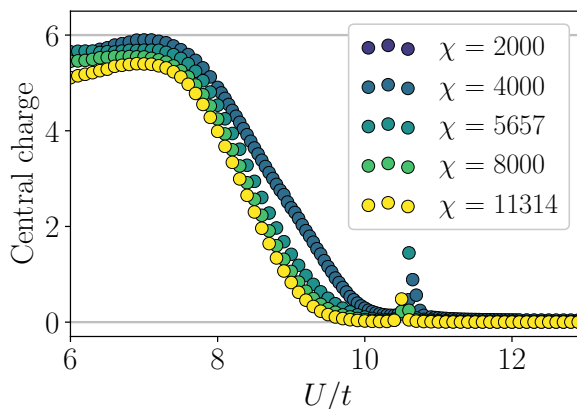


FIG. 11. Central charge as computed using equation (6).

to be converging with increasing bond dimension, as shown in Figure 10, which is indicative of a gapped phase that should have $c = 0$. The apparent nonzero central charge comes from the fact that both the entanglement and the correlation length are still growing very slightly at the accessible bond dimensions.

Another option, then, is to compute the central charge directly from the scaling of entanglement with bond dimension, using^{7–9}

$$S \approx \left(1 + \sqrt{12/c}\right)^{-1} \log(\chi). \quad (6)$$

The central charge computed in this manner is shown vs U/t in Figure 11. In the gapless low- U phase, this is less accurate than the computation of c from scaling with ξ , but at higher U it is indeed more converged. Slices at $U/t = 9$ and 10 in the intermediate phase and $U/t = 13$ in the high- U phase are shown in Figure 12. It is still not completely clear that system is gapped at $U/t = 9$, but that is likely a finite bond dimension effect, as the later point in the same phase, at $U/t = 10$, clearly shows $c = 0$.

VI. YC4 ENTANGLEMENT SPECTRUM DEGENERACY

As reported in the main text, the entanglement spectrum of the ground state on the YC4 cylinder acquires an exact two-fold degeneracy when entering the intermediate phase, at $U/t \approx 8.3$, a fact that we demonstrate here. Recall that the entanglement spectrum is the set of values $\{\log(\lambda_i)\}$ where the $\{\lambda_i\}$ are the coefficients of the Schmidt

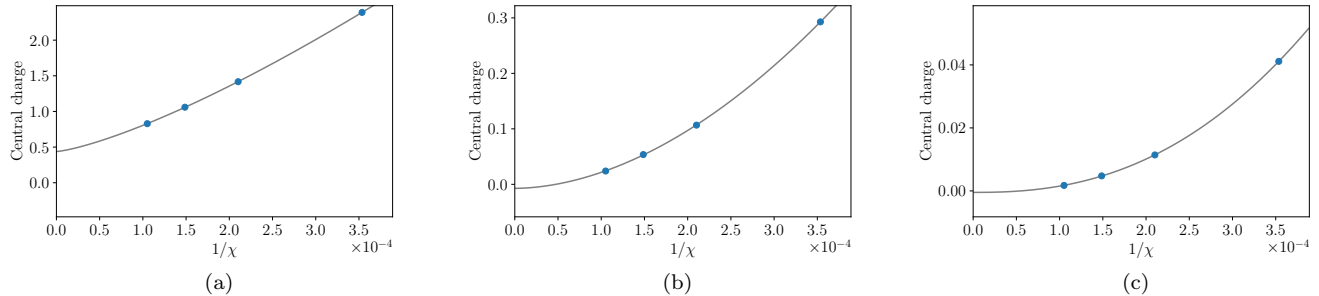


FIG. 12. Central charge vs $1/\chi$, calculated by scaling with bond dimension, for (a) $U/t = 9$, (b) $U/t = 10$, and (c) $U/t = 13$. The latter two clearly extrapolate to 0, suggesting that both the intermediate and high- U phases are gapped. The extrapolation at $U/t = 9$ still appears to go to a nonzero value (approximately $1/2$), but this is likely still a finite bond dimension effect.

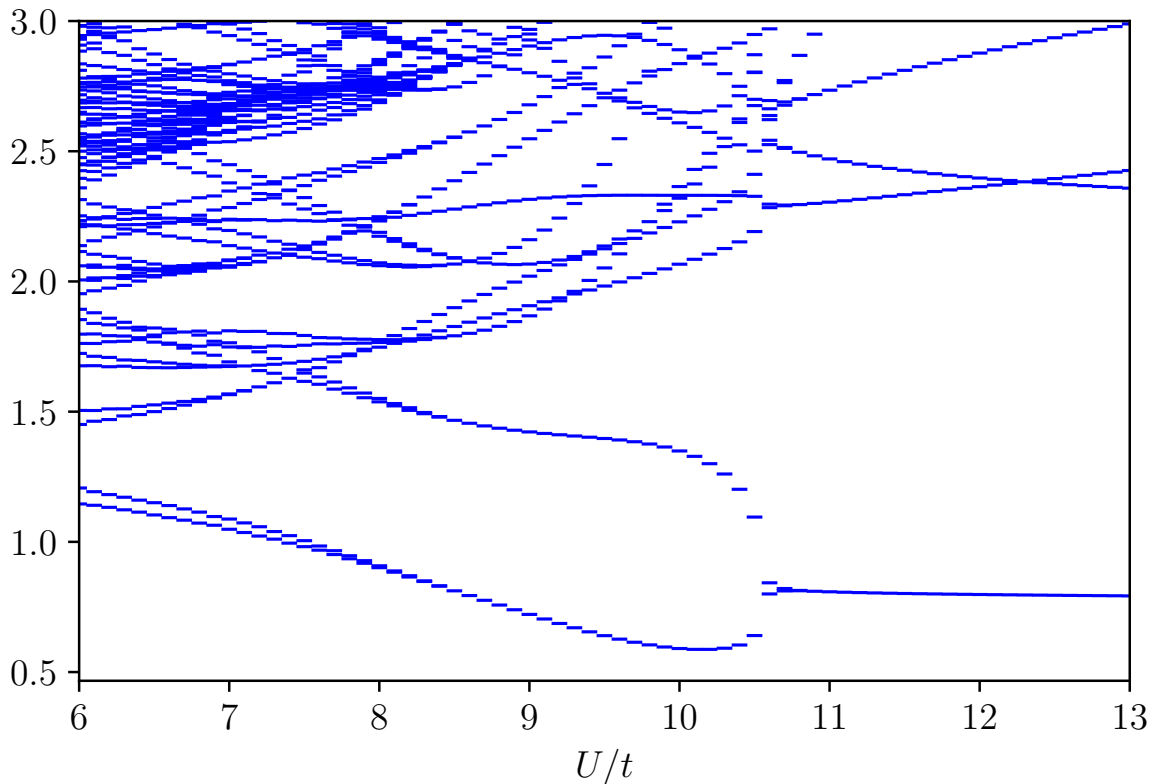


FIG. 13. Entanglement spectrum in the ground state of the YC4 cylinder, as calculated for bond dimension $\chi = 8000$.

decomposition

$$|\psi\rangle = \sum_i \lambda_i |\psi_i^L\rangle |\psi_i^R\rangle \quad (7)$$

for a cut between any two rings of the cylinder¹⁰. Figure 13 shows the low-lying levels in the entanglement spectrum in the ground state as a function of U/t .

The two lowest-lying levels appear to come together somewhere in the vicinity of $U/t = 8$, and then pairs of levels come together at $U/t = 10.6$. This onset of four-fold degeneracy from two-fold degeneracy at $U/t = 10.6$ is visually

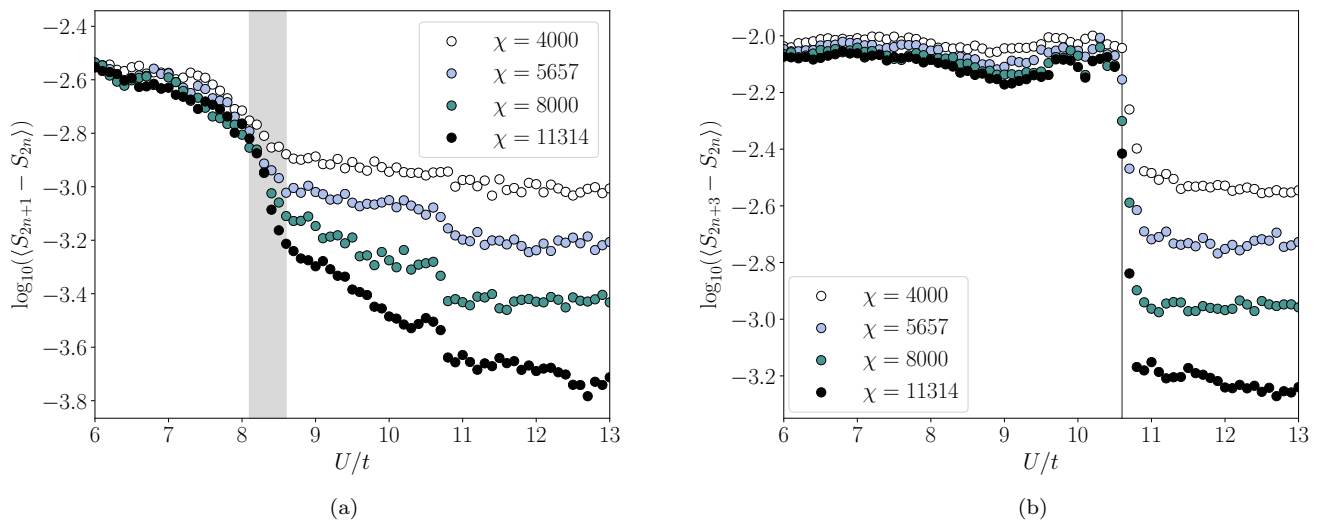


FIG. 14. **(a)** Log of the average separation within pairs of entanglement levels, with 1000 pairs included in the average. The gray bar shows the regions $U/t \in [8.1, 8.6]$; onset of 2-fold degeneracy is somewhere in this region, though the precise location is still difficult to determine. **(b)** Log of the average separation between the top and bottom entanglement levels when grouped into fours, with the lowest 500 groups included (the same total number of entanglement levels). The vertical line at $U/t = 10.6$ is the onset of 4-fold degeneracy.

obvious in the figure: each pair of lines that come together at that point do so at a sharp angle, so that the slope of the entanglement spectrum lines appears discontinuous at that point. The precise location of the first transition, from a nondegenerate entanglement spectrum to two-fold degeneracy, is not clearly visible in the same way.

To more precisely find where the two-fold degeneracy onsets, we take all of the entanglement levels for a given value of U/t and a given bond dimension, and group them into adjacent pairs, with the lowest two levels together, the third and fourth together, and so forth. We then find the separation within each pair, and average the separation over the lowest N pairs, for some large N . (We do not average over all pairs because the highest ones will be inaccurate for any finite bond dimension.) The logarithm of this average can be plotted vs U/t for each bond dimension, which is shown for $N = 1000$ in Figure 14a(a). The curves for different bond dimensions all sit roughly on top of one another until around $U/t = 8$, where they start to deviate. For each bond dimension the separation drops towards 0 before flattening off at some finite average separation; as bond dimension increases, this flattening out happens at successively smaller separations. It is still difficult to identify the exact onset of degeneracy in the infinite bond dimension limit, but it appears to be somewhere within the region highlighted by the vertical gray bar, from $U/t = 8.1$ to 8.6 . The value of $U/t \approx 8.3$ used in Figure 2 of the main text is approximately the center of this region.

For confirmation that this is indeed what a finite bond dimension approximation to an exact degeneracy should look like, we have also followed the same procedure with entanglement levels divided into groups of four, plotting the average separation between the highest and lowest levels in each group, which should go to 0 at the onset of four-fold degeneracy. This is shown in Figure 14(b). This indeed shows essentially the same behavior at $U/t = 10.6$ as does the average pair splitting at $U/t \approx 8.3$, so we believe this is a valid and relatively rigorous way to locate the onset of degeneracy.

VII. METAL TO CSL TRANSITION IN $k = 0$ SECTOR OF YC6 CYLINDER

For the YC4 cylinder, we used finite entanglement scaling to show that the metallic phase is gapless with $c = 6$ (main text) and that the intermediate and high- U phases on that cylinder are gapped (above). For the YC6 cylinder, much larger bond dimensions (about $16\times$ larger) are needed to achieve the same accuracy, so we cannot estimate the central charge accurately. However, if we plot the central charge as estimated using equation (6) for pairs of bond dimensions (as described in section V) as a function of U/t , we can still observe a qualitative change in the behavior of the system at one particular point, as shown in Figure 15a. This behavior is consistent with a gapless metallic phase at low U and a gapped phase at intermediate U .

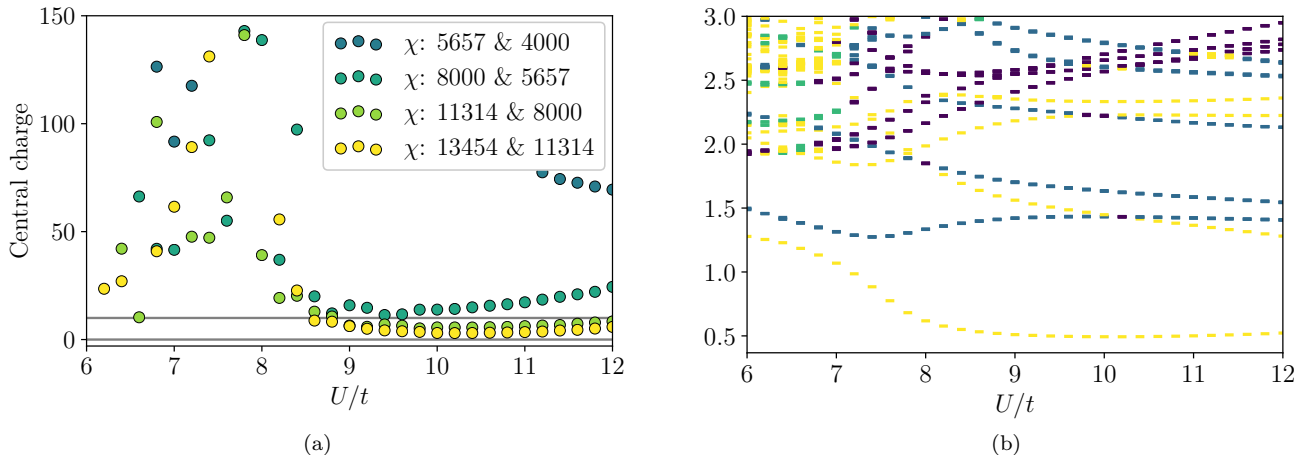


FIG. 15. Evidence for metal to spin liquid transition in the $k = 0$ sector for the YC6 cylinder: **(a)** At $U/t \approx 8.5$, there is a qualitative change in the behavior of the finite entanglement scaling. To the left the scaling of entanglement with bond dimension appears chaotic, which is not surprising for a gapless system when the bond dimension is very small compared with the size of the Hilbert space; to the right the behavior becomes systematic, because the DMRG converges much more accurately even at low bond dimensions when the system is gapped. **(b)** The same transition is also visible in the entanglement spectrum, plotted here for $\chi = 8000$. The dense levels in the upper left are characteristic of a metallic state. At $U/t \approx 7.5$ there is a large increase in the separation between the lowest levels, and the low-lying levels become much more sparse in general, showing a transition into a non-metallic state. (Note that the coloring indicates degeneracy of the levels: yellow is non-degenerate and blue is 3x degenerate).

The transition can also be observed in the entanglement spectrum. Metallic phases characteristically have very densely spaced levels, which as shown in Figure 15b is true for the YC6 cylinder when $U/t \lesssim 8$ but is no longer true beyond that point. Just to the left of that same point, there is a corresponding rapid increase in the separation of the lowest levels; on its own, that feature would not be sharp enough to identify a transition, but in combination with everything else, it provides some additional evidence for the location of the transition.

The two indicators of a transition are slightly displaced from each other, but both are in the vicinity of $U/t \approx 8$, so we identify that region as the approximate location of the transition.

VIII. LABELING THE ENTANGLEMENT SPECTRUM BY QUANTUM NUMBERS

We use a matrix product state with all legs labeled by conserved charges, so that when we perform the Schmidt decomposition as in equation (7), each Schmidt state $|\psi_i^L\rangle$ is an eigenstate of three operators: total momentum around the cylinder, spin up occupation number, and spin down occupation number. We then label the λ_i by the corresponding integer eigenvalues.

However, for iDMRG the left and right Schmidt states extend to infinity, and it is not obvious how these integer charge labels correspond to “physical” values of the charge because, for example, the total spin up occupation is infinite in each of the two halves. Thus our charge labels actually give the total charge relative to some point on the cylinder (arbitrarily chosen as a result of details of the DMRG algorithm) which may be far from the cut we consider in the Schmidt decomposition.

We can fix this ambiguity by subtracting a constant offset from all charge labels so that the net charge on each of the two semi-infinite halves, defined by

$$\sum_i \lambda_i^2 Q_{\lambda_i} \quad (8)$$

where Q_{λ_i} is the charge label of λ_i , is 0. A more rigorous treatment of this subtraction is given in the Supplementary Material of reference 11, section II(B).

After making this correction, each Schmidt value λ_i is labeled by a set of “physical charges” including the momentum and total spin $((n_\uparrow - n_\downarrow)/2)$. The latter may be a half-integer if, as in the semion sector of a chiral spin liquid (CSL), there are fractionalized quasiparticles.

IX. FOUR-FOLD GROUND STATE DEGENERACY

As shown in Figure 3(a) of the main text, for the YC6 cylinder we find low-lying states in two different sectors of momentum around the cylinder per ring. In addition to this near-degeneracy, which as explained in the main text is between the trivial and semion topological sectors, we also observe an additional two-fold degeneracy between the two different possible chiralities.

When finding the ground state using the DMRG method, one begins with some initial matrix product state; if the ground state is not degenerate and the algorithm does not get stuck in a metastable state, the final wave function should be approximately independent of the initial state. If, on the other hand, there are multiple degenerate ground states, the algorithm will converge to one or another of them depending on the initial state used. (It will also tend to converge to minimally entangled states within the ground state manifold and not superpositions of them.¹¹)

In our case, over a wide range of U/t for a bond dimension $\chi = 8000$, we initialized the DMRG with ten different random product states. In the center of the CSL phase, the energies of the final states within each momentum sector varied by up to about 0.01%, meaning that none of the final states were metastable. Although none of the states were numerically identical, they can be separated into two groups within which they are essentially the same, with an overlap per ring of about 0.99998; the overlap between states in opposite groups is about 0.22 per ring. That these two groups correspond to the two possible chiralities of the time-reversal symmetry-breaking phase can be seen from the momentum-resolved entanglement spectra, shown in Figure 16 for representative final states in each of the two groups for each topological sector for $U/t = 9$: the spectra are almost precisely related by $k \rightarrow -k$. (Note that parts (a) and (c) are essentially the same as the left and right respectively of Figure 4(a) of the main text; the main text figures were generated by using the ground states shown here as the initial states for DMRG optimization with a larger bond dimension.)

X. FLUX INSERTION AND THE ENTANGLEMENT SPECTRUM

As described in the main text, we use adiabatic flux insertion to observe a spin Hall effect and confirm that the spin- and momentum-resolved entanglement spectrum matches that of a chiral spin liquid. For the YC4 cylinder, we show here the entanglement spectrum, including how it transforms under flux insertion, and we show the effects of flux insertion more generally including spin pumping and the shifting of phase boundaries. For the YC6 cylinder, we show how the spin- and momentum-resolved entanglement spectrum transforms under adiabatic flux insertion, and we provide some additional evidence regarding adiabaticity and lack of gap closings during flux insertion.

A. YC4 flux insertion

In Figure 4(a) of the main text, we showed spin pumping from flux insertion for $U/t = 10$, in the CSL phase. Compared with the spin pumping for YC6 (Figure 4(b)), there is substantially more deviation from a straight line, which arises because of large shifts in the phase boundaries with flux insertion.

The practical effect of flux insertion is to twist the boundary conditions in the Hamiltonian so that

$$c_{xy\sigma} \rightarrow e^{i(y/n)\sigma\theta/2} c_{xy\sigma}; \quad (9)$$

equivalently, in momentum space around the cylinder each momentum is shifted by $k \rightarrow k \pm \theta/2$, where the + sign is for spin up hopping terms and the - sign for spin down. The smaller the cylinder circumference, the larger an effect this shift will have. (Looking at Figure 1 of the main text, parts (b) and (d), a 4π flux insertion will shift the allowed momentum cuts up by one line; each cut passes through a much larger region of the Brillouin zone when there are fewer lines in total.) Flux insertion thus has an extremely strong effect on the YC4 cylinder, as can be seen by looking at the entanglement spectrum vs U/t at successive values of the flux insertion, shown in Figure 17. Evidently the boundaries of the chiral phase shift, from $U/t \in (\approx 8, 10.6)$ to $U/t \in (\approx 10, \approx 12)$.

This shift in the phase boundaries is clearly apparent if we look at spin pumping at values of U/t such that the system crosses one or more phase boundaries with flux insertion, as shown in Figure 18. With a small amount of flux insertion, $U/t = 9.2$ is close to the straight line for spin pumping, but the phase boundary into the non-chiral phase moves past $U/t = 9.2$ just before 2π flux, leading to the plateau in the center of Figure 18a. At the other extreme, $U/t = 11.0$ is initially in the high- U phase and thus has no spin pumping with flux insertion, but around π flux the phase boundary moves past and it jumps into the chiral phase, showing perfect spin pumping until the phase boundary moves past again in the other direction, at around 3π flux. This is shown in Figure 18b.

(Note that Figure 17 is computed with $\chi = 8000$, whereas Figure 18 is computed with $\chi = 4000$ to allow a higher resolution in the flux with a reasonable amount of computing time, so the phase boundaries do not line up perfectly.

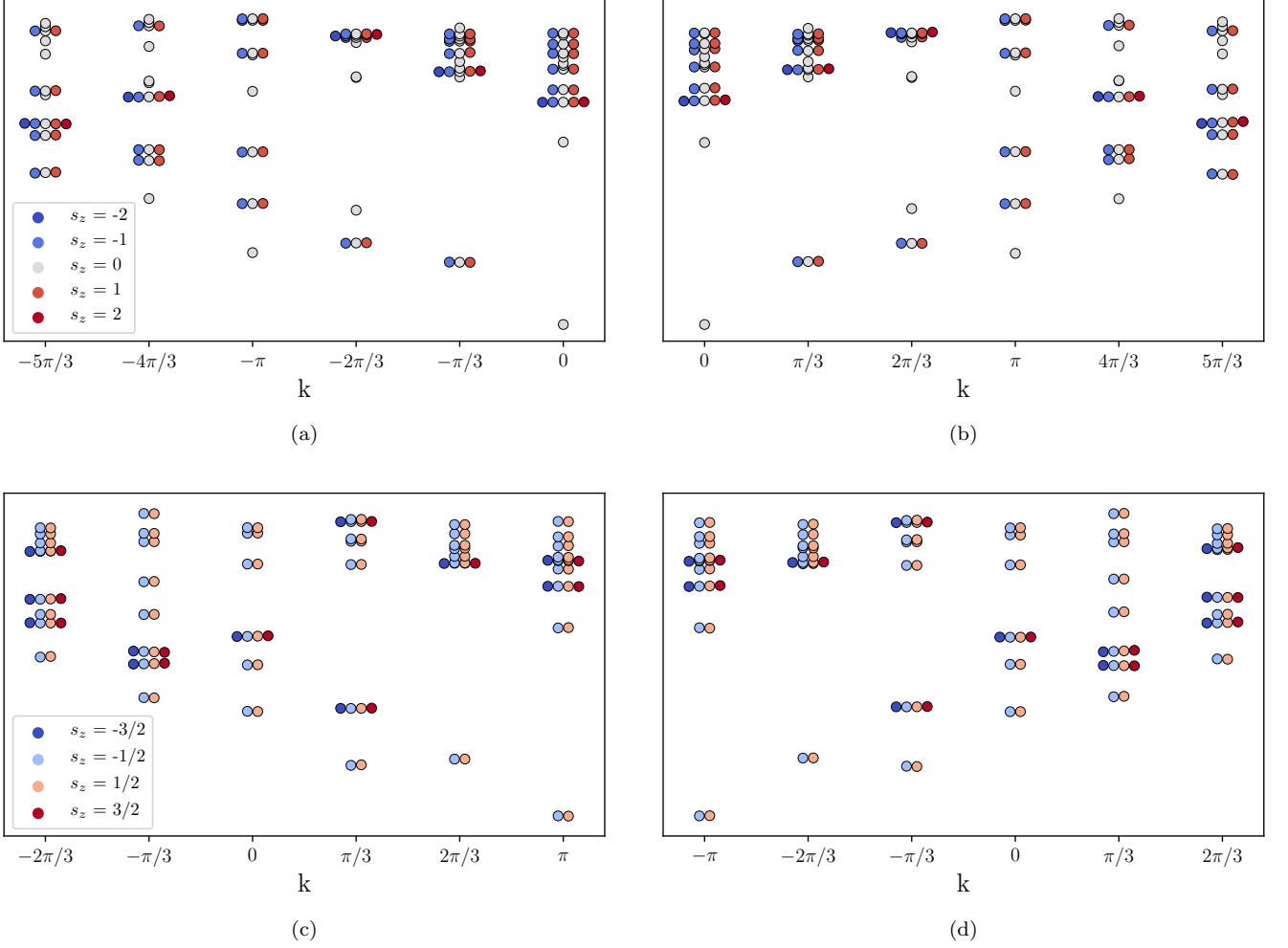


FIG. 16. (Color online) Spin- and momentum-resolved entanglement spectra for the four degenerate ground states of the YC6 cylinder with $U/t = 9$. (a) and (b) show the two chiralities for the $k = 0$ (trivial) sector, and (c) and (d) show the $k = \pi$ (semion) sector.

In particular, for $\chi = 4000$ the chiral phase at 2π flux extends slightly farther to the left than in Figure 17c, so the equivalent of Figure 4(a) of the main text would likely look more like Figure 18a at higher bond dimensions.)

Due to the shifting phase boundaries, the spin- and momentum-resolved entanglement spectrum does not at any one individual value of U/t show a clear evolution from the semion to the trivial sector of a chiral spin liquid with 2π flux insertion. However, if at both 0 flux and 2π flux we take the spectrum for a value of U/t that is in the chiral phase for that value of flux, we do see the expected behavior. Figure 19 shows (a) the spectrum at $U/t = 9.8$ with no flux, corresponding to the semion sector of a CSL, (b) the spectrum at $U/t = 9.8$ with 2π flux, which is no longer in the chiral phase (actually, from Figure 17d it appears to be very slightly chiral, but not enough to be observable here), and (c) the spectrum at $U/t = 11.8$ with 2π flux, in the shifted chiral phase, which shows clearly the expected spectrum of the trivial CSL sector.

B. YC6 flux insertion

For the YC6 cylinder, the boundaries of the chiral phase are much more stable with respect to flux insertion, giving clean results for the spin pumping, as shown in Figure 4(c) of the main text, as well as for the transformation of the spin- and momentum-resolved entanglement spectrum; the latter is shown in Figure 20. Beginning from the semion sector (with the entanglement spectrum shown in Figure 16c), insertion of 2π flux converts to the trivial sector and a further 2π flux converts back to the semion sector.

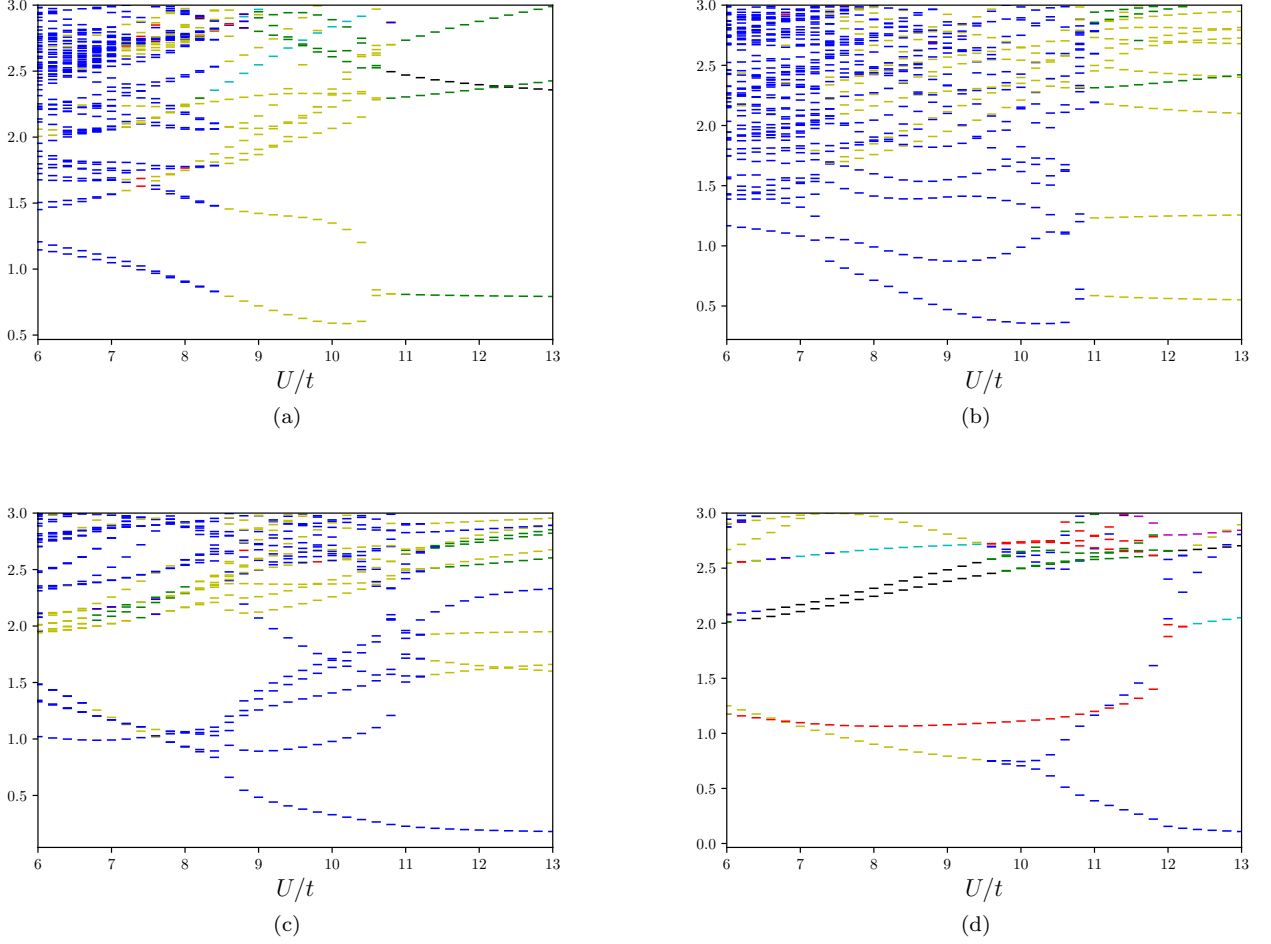


FIG. 17. (Color online) YC4 entanglement spectrum (with $\chi = 8000$) vs U/t for different amounts of flux insertion: **(a)** No flux insertion, **(b)** $2\pi/3$ flux, **(c)** $4\pi/3$ flux, and **(d)** 2π flux. The entanglement spectra are colored by degeneracy of the levels: blue indicates nondegenerate levels, yellow indicates doubly degenerate levels, red is 3x degenerate, and green is 4x degenerate.

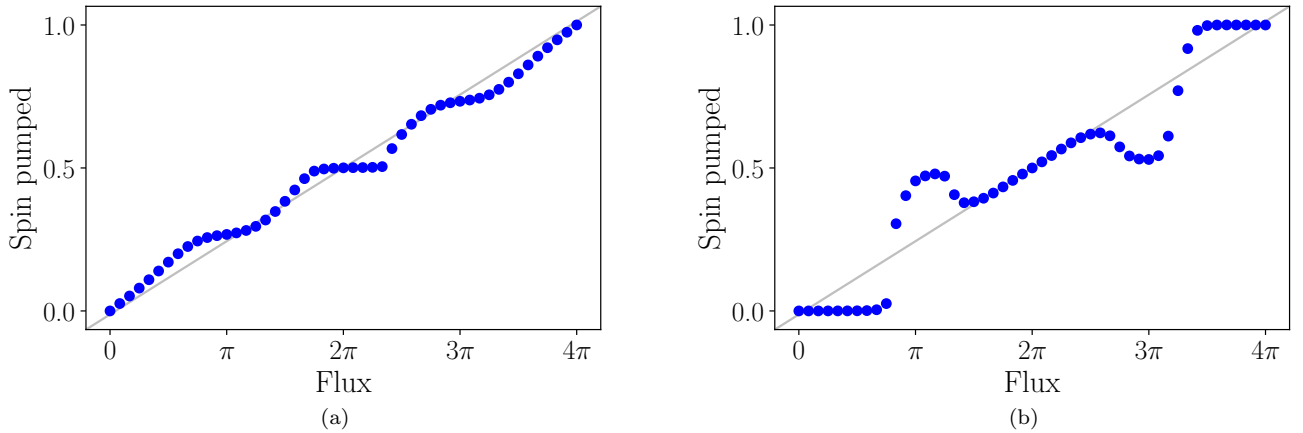


FIG. 18. (Color online) YC4 spin pumping: **(a)** $U/t = 9.2$ and **(b)** $U/t = 11.0$.

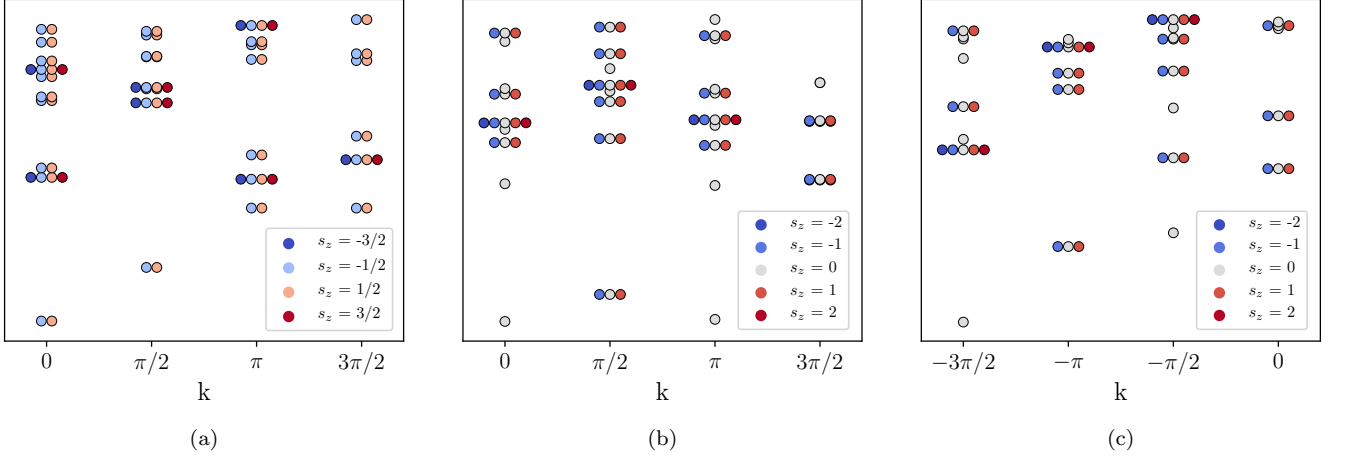


FIG. 19. (Color online) YC4 spin- and momentum-resolved entanglement spectrum with $\chi = 8000$: (a) $U/t = 9.8$, 0 flux; (b) $U/t = 9.8$, 2π flux; and (c) $U/t = 11.8$, 2π flux.

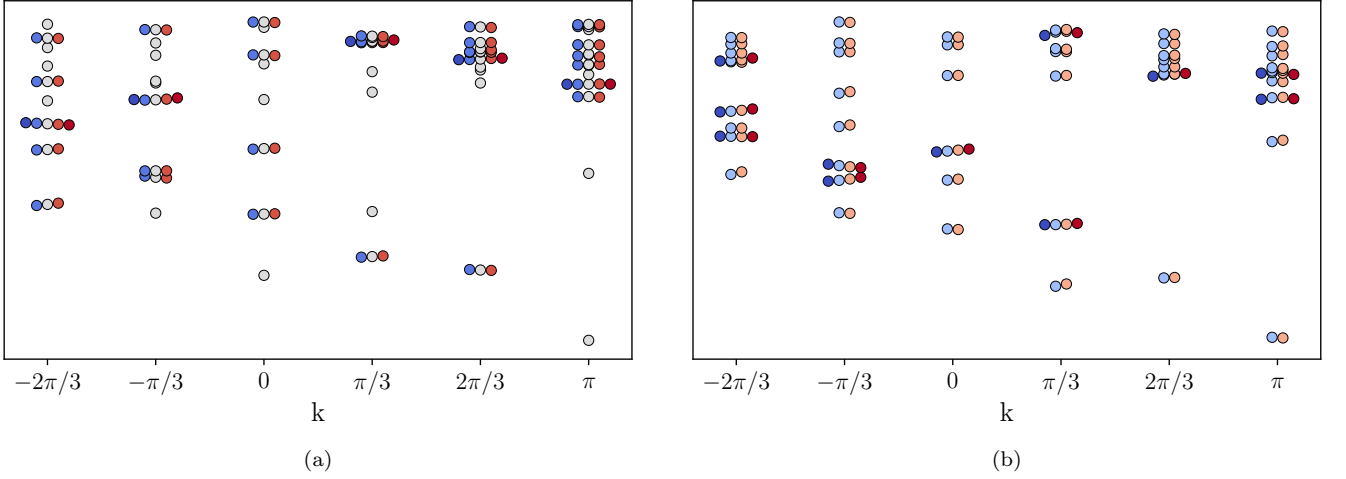


FIG. 20. (Color online) The transformation of the YC6 spin- and momentum-resolved entanglement spectrum with flux insertion for $U/t = 9$, beginning in the semion sector (as shown in Figure 16c): (a) 2π flux converts the system to the trivial sector (compare with Figure 16a) and (b) an additional 2π flux, or 4π total, returns to the initial state.

Although the flux insertion works more cleanly in the chiral phase for YC6 than for YC4, the boundary between the chiral and spin-ordered phases does still shift to the right. Consequently, the spin pumping in the low- U part of the ordered phase looks qualitatively similar to the one shown in Figure 18b for the YC4 cylinder; This is shown for $U/t = 12$ in Figure 21. The shifted boundary is related to the fact that the chiral order parameter does not vanish in the high- U phase for the $k = 0$ sector, as shown in Figure 3(c) of the main text.

Deep in the chiral phase, where the flux insertion has the expected effect of interchanging the two ground state sectors of the CSL, it is also worth considering some additional evidence for the stability of the phase and in particular for the absence of nodal gapless points in the Brillouin zone. To this end, we show in Figure 22, for the same U/t used for plotting the spin pumping and entanglement spectra in Figure 4 of the main text, the ground state energy and the entanglement between two rings as a function of flux insertion. The energy changes by only about 1/3 of a percent, and while the entanglement varies by about 6%, it never increases above the value in the ground state of the $k = \pi$ sector, as it likely would if there were a gapless point in the Brillouin zone. (As a caveat, the resolution in the flux insertion is still relatively low, so we could still be missing a local closing of a small gap. We also do not have data from multiple bond dimensions, and $\chi = 8000$ used here may not be large enough to guarantee that a gapless state would have a larger entanglement than a gapped one, particularly if it is gapless only at isolated points.)

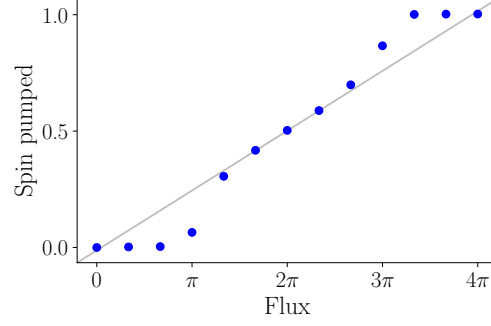


FIG. 21. Spin pumping for the YC6 cylinder in the low- U region of the spin-ordered phase, showing that the phase boundary shifts to the right with flux insertion, passing $U/t = 12$ at about $4\pi/3$ flux.

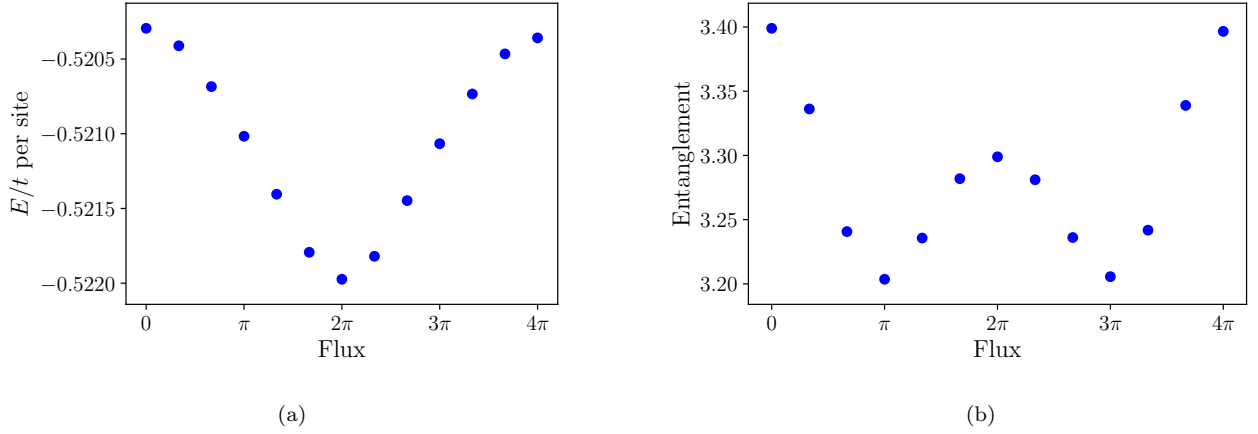


FIG. 22. Stability of the chiral phase with respect to flux insertion for the YC6 cylinder at $U/t = 9$: (a) ground state energy and (b) entanglement between rings.

* aszasz@berkeley.edu

¹ S. R. White, *Phys. Rev. Lett.* **69**, 2863 (1992).

² U. Schollwöck, *Annals of Physics* **326**, 96 (2011), January 2011 Special Issue.

³ S. Yan, D. A. Huse, and S. R. White, *Science* **332**, 1173 (2011).

⁴ Philippe Francesco, Pierre Mathieu, and David Sénéchal, *Conformal Field Theory* (Springer-Verlag New York, 1997).

⁵ C. Hubig, J. Haegeman, and U. Schollwöck, *Phys. Rev. B* **97**, 045125 (2018).

⁶ P. Calabrese and J. Cardy, *Journal of Statistical Mechanics: Theory and Experiment* **2004**, P06002 (2004).

⁷ L. Tagliacozzo, T. R. de Oliveira, S. Iblisdir, and J. I. Latorre, *Phys. Rev. B* **78**, 024410 (2008).

⁸ F. Pollmann, S. Mukerjee, A. M. Turner, and J. E. Moore, *Phys. Rev. Lett.* **102**, 255701 (2009).

⁹ B. Pirvu, G. Vidal, F. Verstraete, and L. Tagliacozzo, *Phys. Rev. B* **86**, 075117 (2012).

¹⁰ H. Li and F. D. M. Haldane, *Phys. Rev. Lett.* **101**, 010504 (2008).

¹¹ M. P. Zaletel, R. S. K. Mong, and F. Pollmann, *Phys. Rev. Lett.* **110**, 236801 (2013).